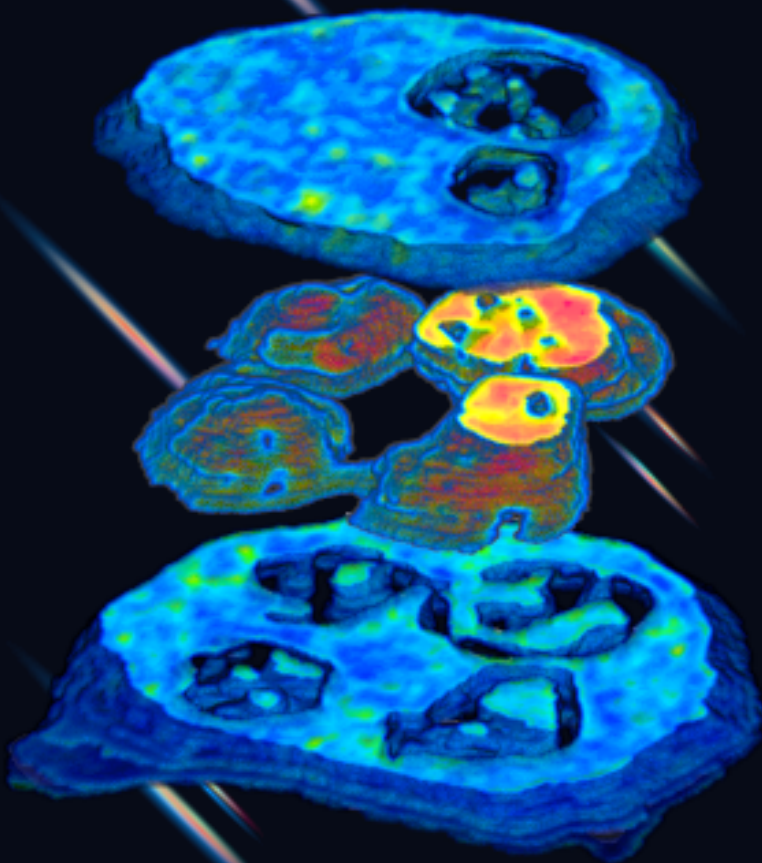


Linköping Studies in Science and Technology
Dissertation No. 2518

Cellular Imaging and Work Function Mapping:

Neutrophils and Nanoparticle Guided
Extracellular Traps

Filip Genander



Linköping Studies in Science and Technology. Dissertations No.
2518

**Cellular Imaging and
Work Function Mapping:
Neutrophils and Nanoparticle Guided
Extracellular Traps**

Filip Genander



Department of Physics, Chemistry and Biology, Division of Molecular
Surface Physics and Nanoscience
Tekniska Fakulteten
Linköpings universitet, SE-581 83 Linköping, Sweden
Linköping 2026

Supervisor:

Kajsa Uvdal

Professor

Department of Physics, Chemistry and Biology

Co-supervisor:

Caroline Brommesson

Associate Professor

Department of Physics, Chemistry and Biology

Andreas Skallberg

Assistant Professor

Department of Physics, Chemistry and Biology


Faculty opponent:

Maria Messing

Professor

Head of the Department of Microtechnology and Nanoscience,
Chalmers

© Filip Genander, 2026

 Except where otherwise noted, this work is licensed under a Creative Commons Attribution 4.0 International license. To view a copy of this license, visit:

<https://creativecommons.org/licenses/by/4.0/>

Printed in Sweden by LiU-tryck, 2026

ISBN 978-91-8118-540-9 (print)

ISBN 978-91-8118-541-6 (PDF)

<https://doi.org/10.3384/9789181185416>

ISSN 0345-7524

-Cover Image: The cover image is a work function-mapped volume of a neutrophil. The background illustrates the threads formed by iron oxide nanoparticles and neutrophil extracellular traps under a magnetic field.

“Just remember, when you’re over the hill, you begin to pick up speed.”
– Charles M Schultz, Creator of Peanuts

Abbreviations

(ARPES)	Angle-Resolved Photoemission Spectroscopy
(DAMPs)	Damage associated molecular patterns
(ECM)	Extracellular matrix
(FeOx)	Iron oxide
(FoV)	Field of view
(FT-IR)	Fourier Transform Infrared Spectroscopy
(GSDMD)	Gasdermin D
(HAT)	Histone acetyltransferase
(IDEA)	Imaging double energy analyzer
(IMFP)	Inelastic mean free path
(IR)	Infrared
(IRAS)	Infrared reflection absorption spectroscopy
(MNP)	Magnetic nanoparticles
(MPO)	Myeloperoxidase
(MRI)	Magnetic resonance imaging
(NE)	Neutrophil elastase
(NETs)	Neutrophil extracellular traps
(NP)	Nanoparticles
(PAD4)	Peptidylarginine deaminase 4
(PAMPs)	Pathogen-associated molecular patterns
(PEEM)	Photoemission electron microscopy
(PES)	Photoelectron spectroscopy
(PMA)	Phorbol myristate acetate
(PMN)	Polymorphonuclear leukocytes
(PRRs)	Pattern recognition receptors
(PFA)	Paraformaldehyde
(ROS)	Reactive oxygen species
(SEM)	Scanning electron microscopy
(SPION)	Superparamagnetic iron oxide nanoparticles
(UPS)	Ultraviolet Photoelectron Spectroscopy
(UV)	Ultraviolet
(XPS)	X-ray Photoelectron Spectroscopy

Abstract

Advanced microscopy and imaging techniques are essential for investigating cellular and subcellular architecture and chemical composition. In this thesis, **Photoemission Electron Microscopy (PEEM)** is developed and applied as a surface- and chemically sensitive imaging modality for biological systems, with a particular focus on neutrophils. **Neutrophils** are the most abundant white blood cells in humans and constitute a first line of defence in the innate immune system. Upon activation, they perform key antimicrobial functions, including phagocytosis, degranulation, and the release of **neutrophil extracellular traps (NETs)**, which trap, immobilize, and neutralize invading pathogens using DNA and antimicrobial agents.

In this work, NETs formation in combination with iron oxide (FeO_x) nanoparticles is investigated, including the **magnetically guided assembly of linear and cross-shaped NETs- FeO_x nanoparticle μ -threads**, induced by magnetic nanoparticles and externally applied magnetic fields. These engineered extracellular structures hold potential for materials with intrinsic antibacterial properties and, under magnetic control, exhibit a high degree of orientational order. The ability to impose controlled macroscopic alignment on DNA-based structures further suggests opportunities for the development of robust, oriented macromolecular systems, with relevance for structured organic and conjugated materials.

Work-function mapping based on surface-sensitive contrast in PEEM is a powerful and well-established technique in surface physics and materials science; however, its application in the life sciences, particularly for subcellular imaging, remains largely unexplored. To increase the information content of cellular imaging, this thesis

introduces a photoemission-based strategy that integrates **three-dimensional spatial reconstruction** with **pixel-resolved spectral (work-function) contrast**, enabling quantitative insight into cellular composition and organization. Local variations in the work function provide intrinsic contrast between subcellular structures based on their molecular composition, allowing visualization of the polylobulated nuclei, intracellular granules, and membrane structures of neutrophils.

The thesis further includes the development and surface modification of gadolinium-incorporated cerium oxide nanoparticles for use as contrast agents in magnetic resonance and X-ray imaging. Two functionalization strategies are presented to enable targeting and therapeutic functionality. X-ray Photoemission Spectroscopy (XPS) is employed for chemical characterization of both nanoparticles and biological structures, highlighting the broader potential of photoemission-based methods within the life sciences.

Populärvetenskaplig sammanfattning

Idag används en rad mikroskopi- och avbildningsmetoder för att studera morfologi och sammansättning hos cellulära strukturer. Möjligheten att visualisera cellers inre delar, den så kallade subcellulära arkitekturen, med nya verktyg öppnar upp för nya perspektiv på cellens funktion och biologiska processer.

Konventionella mikroskopimetoder utnyttjar ofta fysiska egenskaper såsom variationer i densitet, reflektion, absorption och ljusgenomsläpplighet för att skapa kontrast. När objekt blir mindre än den våglängd som används begränsas upplösningen, och färgkontrast blir otillräcklig. Behovet av mer information från varje bild har lett till utvecklingen av avancerade metoder, såsom Photoemission Electron Microscopy (PEEM) och tredimensionell mappning. Genom att kombinera rumslig 3D-information med spektraldata i varje pixel kan man skapa "fyrdimensionella" avbildningar som ger kvantitativ insikt i cellers kemiska sammansättning och struktur. PEEM används traditionellt för inorganiska material som halvledare, katalysatorer och magnetiska ytor. Metoden bygger på att skillnader i utträdesarbete, det vill säga den energi som krävs för att frigöra en elektron från ytan, genererar bildkontrast. Utträdesarbetet är ytspecifikt och påverkas av materialets kemiska sammansättning, molekylära struktur och ytans tillstånd. Kartläggning av utträdesarbetet via ytkänslig fotoemissionskontrast är väl etablerad men är fortfarande i stor utsträckning outforskad inom livsvetenskaperna. Denna metod erbjuder därför spännande möjligheter att komplettera befintliga mikroskopiska tekniker när det gäller avbildning av celler och deras subcellulära arkitektur.

Ett särskilt fokus i detta arbete ges till neutrofiler, som hos oss människor är de mest förekommande vita blodkropparna och en av de första celltyperna som aktiveras vid en immunrespons. Neutrofiler använder tre huvudsakliga försvarsmekanismer: degranulering,

fagocytos och extracellulära nät av DNA (NETs). Avhandlingsarbetet demonstrerar hur PEEM kan utvecklas som verktyg för avbildning och karaktärisering av både celler och extracellulära fällor. Eftersom olika organeller har olika molekyllär sammansättning och därmed olika utträdesarbete, kan utträdeskartläggning isolera specifika delar av cellen. I artikel III visas detta med fokus på den separerade cellkärnestrukturen, som är karaktäristisk för neutrofiler.

Vid aktivering kan neutrofiler frisätta sitt DNA, och därmed bilda extracellulära nät (NETs) som fångar inkräktare. Dessa nät är beklädda med antimikrobiella molekyler som effektivt oskadliggör patogener. I denna avhandling används Photoemission Electron Microscopy (PEEM) för att studera de subcellulära strukturerna såsom formen på den polynukleära kärnan, cellmembranet och kärnmembranet.

I detta arbete visas hur linjära NETs kan skapas genom att exponera neutrofiler för magnetiska nanopartiklar och därefter applicera ett kontrollerat externt magnetfält. Vi visar att isolerade NETs tillsammans med magnetiska järnoxidnanopartiklar under externt magnetfält kan bilda välordnade linjära och korsformade NETs-FeO_x μ -trådar. Metoden öppnar för skräddarsydda, magnetiskt styrda DNA-nätverk med potential som kontrollerade antibakteriella strukturer och funktionell molekyllär armering.

Nanopartiklar används även som kontrastmedel i både skiktröntgen och magnetresonanstomografi. Det finns idag ett behov av att skapa kontrastmedel som kan tas i låga doser med terapeutiska och målsökande egenskaper. Vi har därför visat på två modifieringsmetoder av nanopartiklar av ceriumoxid inkorporerade med gadolinium för att möta dessa behov. Metod 1 täcker nanopartikeln i ett tunt polymerlager kopplat till en molekyllär varpå man kan klicka fast antikroppar riktade mot till exempel cancer. Metod 2 använder plasma av acetylen, kväve och argon för att inkapsla flera nanopartiklar tillsammans i ett kollager med kemiska grupper som lämpar sig för att fästa antikroppar vid.

Med hjälp av fotoemission med röntgenljus, så kallad röntgenfotoelektron-spektroskopi (X-ray Photoemission Spectroscopy XPS) kan vi få fram grundämnesspecifik information vid karaktärisering av nanopartiklar och celler. Information som oxidationstal på cerium eller den kemiska miljön för kol är viktiga för att beskriva partiklarnas egenskaper. Detta belyser potentialen av fotoemission som karaktärisering och avbildningsmetod för livsvetenskapen.

Acknowledgement

All journeys have a beginning, and this one started with a pandemic, what better time than this to start a PhD and explore the curiosities of science. Research is certainly a unique occupation with heights to the sky and lows to the abyss. However, what I will remember the most are all the moments in between and the people giving life to these moments. For what is the chit chat in the lab, a sour cup of coffee in the morning or a leg stretcher without colleagues to share it with?

To Kajsa, my main supervisor, I would like to thank you for seeing my interests and skills and letting me develop in my own direction during all these years. Thank you for all that you have taught me over the years. By now I think you and I and Andreas can put up the baking shields blindfolded in the middle of the night. Carro, my first co-supervisor, thank you for doing such a good job with Agora, being the structured adult in the room and your cheeriness. To Andreas, (ärkebonden) my second co-supervisor, beside everything work related you have helped me with, I want to thank you for all the cups of coffee in front of Christopher Odd and the walks to work. To Zhangjun my “not on paper supervisor”, thank you for always helping me out with good advice.

To the rest of the group, I could not have asked for better colleagues. Anna, you took me under your wings when I was new and guided me on this crooked journey. Julia and Martin, name me a more dynamic duo, you are the fun which gives an inner satisfaction and is the foundation upon which our group rests. Ida, it has been my privilege to show you the ropes and I wish you would have started in our group sooner. Thirza, thank you for the many walks we have shared. Fredrik for all the lunches in the “sunny corner”. Jiwen, thank you for always being so nice and sincere. Johan, thank you for our great

conversations. Wei thank you for teaching me Chinese with such patience. Thank you Kalle for all that you have taught me.

I want to thank the division fika group for all conversations. All the Agora members, you are too many to count but none the less good memories together. Thank you, Maria, for helping me out on short notices and cheering me on.

Philip you are the Sam to my Frodo, you could not carry my PhD but you could carry me. It has been unreal to have such a close friend as a colleague, and I hope we will continue our journey together.

Without the support of my friends, near and far, these years would not have been the same! Thank you all for cheering me on. Thank you to my family and relatives for loving me no matter what and inspiring me to be the best version of myself.

Agnes my wife, I don't think I can describe here how much you mean to me, that would require a thesis on its own. Thank you for always standing beside me, believing in me and putting in an immense effort supporting me these past months. Bosse my son, you are the work that makes me function. Thank you for putting everything into perspective. I will always love you infinitely.

All journeys have an end. At this journey's end, I stand, not as I arrived, but not only with more textbook knowledge, but changed in the way I think, feel and evaluate. Thank you to all who have been on this journey with me.

List of papers

I. **Superparamagnetic Nanoparticle-Guided Alignment of Neutrophil Extracellular Traps**

Andreas Skallberg, Filip Genander, Kalle Bunnfors, Caroline Brommesson and Kajsa Uvdal.

In manuscript

Author contribution

FG took part in both preparation of the cell-experiments as well as experiments when aligning iron oxide nano-threads. FG contributed to the analysis and was involved in the scientific discussion.

II. **Fabrication and characterization of Neutrophil extracellular traps- FeO_x nanoparticle μ -threads**

Filip Genander, Ida Hofvander, Andreas Skallberg, Caroline Brommesson and Kajsa Uvdal.

In manuscript

Author contribution

FG took part in planning the experimental setup and performed cell experiments and sample preparation. FG performed characterisation by means of IR, SEM, DLS. FG partly performed, DNA concentration determination, magnetic field strength and fluorescence microscopy. FG developed a small chamber of his own design, tailor-made for these experiments. FG performed statistical analysis and took part the work function mapping analysis. FG took part in the writing of manuscript.

III. **4D Work-Function Mapping of Neutrophil Subcellular Architecture**

Filip Genander, Andreas Skallberg and Kajsa Uvdal.

In manuscript

Author contribution

FG was strongly involved in planning the project. FG performed all the cell experiments. FG performed characterisation by means of bright field microscopy and fluorescence microscopy. FG performed a major part of the image processing and analysis. FG wrote main part of the manuscript.

IV. **EGFR-Targeting Cerium–Gadolinium Core–Shell Nanoprobes for Imaging Head and Neck Squamous Cell Carcinoma**

Anna du Rietz, Karin Roberg, Filip Genander, Per O.Å.

Persson, Andreas Skallberg, Caroline Brommesson,

Zhangjun Hu and Kajsa

Submitted to ACS OMEGA.

Author contribution

FG was involved in the XPS experiments and performed XPS data analysis and following interpretation, and FG contributed to corresponding of the manuscript.

V. **Coating and Functionalization of Multi Core Cerium–Gadolinium Oxide Nanoparticles via Plasma-Enhanced Chemical Vapor deposition**

Anna du Rietz, Igor Zhirkov, Filip Genander, Alba Abeledo De La Vega, Clara Tran, Pierfrancesco Pagella, Andreas Skallberg, Caroline Brommesson, Marcela Bilek, Johanna Rosén, Kajsa Uvdal.

In manuscript

Author contribution

FG was involved in the XPS experiments and performed XPS data analysis and following interpretation, and FG contributed to corresponding of the manuscript.

Table of Contents

Abstract	vi
Populärvetenskaplig sammanfattning	ix
Acknowledgement	xiii
List of papers	xv
Table of Contents	xix
1 Introduction.....	1
1.1 Superparamagnetic iron oxide nanoparticles (SPION)	1
1.2 Neutrophil granulocytes	3
1.2.1 Intracellular content.....	3
1.2.2 Migration	4
1.2.3 Endocytosis and microbial effector functions	5
1.2.4 Neutrophil Extracellular Traps	7
1.3 Neutrophils and Nanoparticles.....	10
1.4 Photoemission	12
1.4.1 Electron excitation.....	13
1.4.2 Electron propagation.....	14
1.4.3 Electron transmission	15
1.5 Work function	16
2 Methods.....	21
2.1 Neutrophil and NETs isolation.....	21
2.1.1 Neutrophil Isolation	21
2.1.2 NETs Isolation	22
2.2 NanoESCA.....	23
2.2.1 PEEM.....	24
2.2.2 X-ray photoelectron spectroscopy	25
2.2.3 Imaging XPS and energy filtered PEEM	28
2.3 Image Processing.....	30
2.3.1 WF mapping.....	30
2.3.2 Non-isochromaticity.....	31
2.3.3 Schottky effect.....	32
2.3.4 4D work function mapping	33
2.4 Infrared reflection absorption spectroscopy (IRAS).....	36
2.5 SEM	42

2.6 Fluorescence microscopy	43
2.6.1 Fluorescence	43
2.6.2 <i>Structure of a microscope</i>	46
2.6.3 <i>Measuring μ-Threads</i>	47
Summary of Papers	50
Future Outlook	56
References	59

Chapter 1

1 Introduction

1.1 Superparamagnetic iron oxide nanoparticles (SPION)

Iron oxide nanoparticles that exhibit superparamagnetism are widely used in biomedical applications. Important examples include *in vivo* contrast enhancement in Magnetic Resonance Imaging (MRI) and magnetic sensing for *in vitro* diagnostics.¹ Additional applications include the targeted delivery of small-molecule drugs, magnetic hyperthermia for cancer therapy, applications in immunotherapy, and their use as adjuvants in vaccine formulations.²⁻⁷

Spin is an intrinsic property of the electron, similar to its mass and electric charge. It represents a form of intrinsic angular momentum carried by elementary particles. The term “spin” originates from early theoretical models in which the electron was imagined as a charged particle rotating about its own axis. However, modern quantum mechanics shows that electron spin is not a literal rotation but rather a fundamental quantum property.⁸

The connection between spin and magnetism arises because an electron with spin possesses a magnetic dipole moment. In atoms, electrons possess both orbital momentum, originating from their motion around the nucleus, and spin angular momentum, which is intrinsic to the electron.⁸ Both contributions give rise to the atomic magnetic moment, although in many materials the spin contribution is dominant.⁹

When atoms are arranged in a crystalline solid, interactions between the magnetic moments of electrons can cause them to align in regions known as magnetic domains. The magnetic properties of these domains depend on the relative alignment of the atomic spins. Consequently, the collective alignment of electron spins determines the net magnetization of the domain.⁹

Ferrimagnetism arises from an antiparallel alignment of atomic spins with unequal magnetic moments in the opposing directions. As a result, the magnetic moments do not completely cancel, producing a net magnetization.⁹

Several iron oxide phases exhibit different magnetic properties. Two of the most relevant phases are magnetite and iron(III) oxide. Magnetite, Fe_3O_4 (iron(II,III) oxide), is a ferrimagnetic material and is the iron oxide used in this thesis. Iron(III) oxide (Fe_2O_3) occurs in multiple crystallographic forms. The α -phase, $\alpha\text{-Fe}_2\text{O}_3$ (hematite), exhibits weak ferromagnetic or antiferromagnetic behaviour, whereas the γ -phase, $\gamma\text{-Fe}_2\text{O}_3$ (maghemite), is ferrimagnetic.¹⁰

When the particle size decreases to the nanoscale, the magnetic behaviour changes significantly. At sufficiently small sizes, magnetic nanoparticles can consist of a single magnetic domain. In this state the entire particle behaves as a single magnetic moment rather than containing multiple domains with different magnetization directions. The nanoparticles thus exhibit superparamagnetic properties, meaning that the nanoparticles do not act as small permanent magnets but become magnetized only in the presence of an applied external magnetic field.¹¹

1.2 Neutrophil granulocytes

Neutrophil granulocytes (Neutrophils) are at the first line of defense against fungal and bacterial infections and are a key component of the innate immune system. Neutrophils are equipped with a variety of antimicrobial agents including reactive oxygen species and hydrolytic enzymes which break down pathogens chemically. These agents are released from granules, small vesicles derived from lipid membranes. Neutrophils also respond to pathogens through phagocytosis (engulfing) and by releasing their DNA to form a web known as neutrophil extracellular traps (NETs), a process that will be covered more extensively in this thesis.¹²⁻¹⁴

The name neutrophil derives from the staining characteristics that the cells retained when first classified. Whereas basophilic white blood cells stain dark blue and eosinophilic white blood cells stain bright red, neutrophils stain a neutral pink.¹⁵ In literature, the term polymorphonuclear leukocytes (PMN) is often used describing the nuclear structure.¹⁶⁻¹⁸

The role of neutrophils began to be uncovered in the 1890's by Elie Metchnikoff, who proposed a role of microbial digestion after observing that phagocytic cells migrated toward injuries in starfish embryos.¹⁹

1.2.1 Intracellular content

Neutrophils' most striking feature is the multiple lobules. Neutrophils contain three different cell type-specific intracellular granules and secretory vesicles originating from endocytosis^{12,20}. Additionally,

neutrophils have very few mitochondria, emphasizing their role as expendable, highly potent cells, relying on large numbers to combat pathogens¹².

1.2.2 Migration

A key feature of neutrophils is the ability to migrate in response to inflammation and infection. Several gradient-dependent mechanisms guide cell movement, including chemotaxis (movement in response to chemical gradients), haptotaxis (movement toward a gradient of adhesion sites or chemo-attractants on a surface such as the extracellular matrix (ECM)), durotaxis (movement in response to a gradient of surface stiffness), and galvanotaxis (movement along an electric charge gradient).²¹⁻²⁴ Neutrophils show three modes of migration or motility modes, gripping and pulling, pushing and squeezing and thirdly a swim-like action.^{25,26}

Gripping and pulling (mesenchymal migration) requires adhesion. When the cell extends actin -rich protrusions at the leading edge, it forms adhesion with the intended surface to crawl along it.²⁷ Integrins and selectins expressed on the neutrophil membrane bind to ligands expressed on other cells or the ECM. The cytoskeleton then exerts a pulling force helping the cell crawl on the surface²⁸.

Amoeboid migration, which involves pushing and squeezing, requires minimal or no adhesion. This form of movement is characterized by the deformation of the cell membrane at the front driven by actin rich pseudopodia (membrane protrusions), hydrostatically generated blebs and uropods (the trailing rear of the cell) to facilitate the retraction of the cell's rear.²⁹

A study published in 2010 reported that neutrophils are able to swim, explained by a treadmilling motion of paddle proteins at the cell membrane.²⁶

1.2.3 Endocytosis and microbial effector functions

Neutrophils recognize pathogens through pattern recognition receptors (PRRs) which are expressed on the cell surface as a form of the innate immune system. These receptors bind to molecules characteristic of pathogens known as pathogen-associated molecular patterns (PAMPs). The neutrophils can also detect molecules released when the host tissue is damaged, referred to as damage associated molecular patterns (DAMPs). Additionally, neutrophils can identify pathogens that have been coated with antibodies or complement proteins, a process known as opsonization²⁸. It has been demonstrated how the uptake of iron oxide “nanoworms” in leucocytes is dependent on opsonization of complement proteins.³⁰

Neutrophils may also assess the size of microbes and alter their response accordingly. Smaller yeast particles $\sim 5\mu\text{m}$, which are easily phagocytosed, lead to intracellular release of reactive oxygen species (ROS) and reduces the recruitment of additional neutrophils. In contrast, larger hyphae filament of the same yeast $> 100\mu\text{m}$ generates ROS extracellularly which promotes the recruitment of more neutrophils to the site of infection.³¹

Neutrophils employ three major effector functions used as a defense against pathogens: phagocytosis, degranulation and NETosis. During phagocytosis the cell-membrane is wrapped around the pathogen, internalizing it into a compartment called the phagosome, where it can be chemically degraded.^{14,32}

When examining neutrophils at high magnifications using electron microscopes it is evident that neutrophils are filled with many vesicles³³. These vesicles are granules, lipid bound membrane containers containing biologically active substances. These granules can be classified into four main categories.³² Azurophilic (primary) granules are the largest, measuring approximately 0.3 μm in diameter and contain key proteins such as: myeloperoxidase (MPO), lysozyme, defensins and neutrophil elastase (NE). Specific (secondary) granules are smaller, around 0.1 μm and lack MPO but are characterized by the presence of glycoprotein lactoferrins. Gelatinase (tertiary) granules are even smaller than specific granules and do not contain MPO. Tertiary granules' primary function is to store metalloproteases. The fourth category consists of secretory vesicles, which are endocytosed. These vesicles contain plasma derived proteins and serve as important storage compartments for membrane bound molecules involved in neutrophil migration.^{34,35}

Neutrophil extracellular traps (NETs) physically trap bacteria and are coated with antimicrobial agents. The process of NET formation, is activation dependent and involves key factors such as myeloperoxidase MPO, neutrophil elastase NE, peptidylarginine deaminase 4 (PAD4) and gasdermin D (GSDMD)¹².

1.2.4 Neutrophil Extracellular Traps

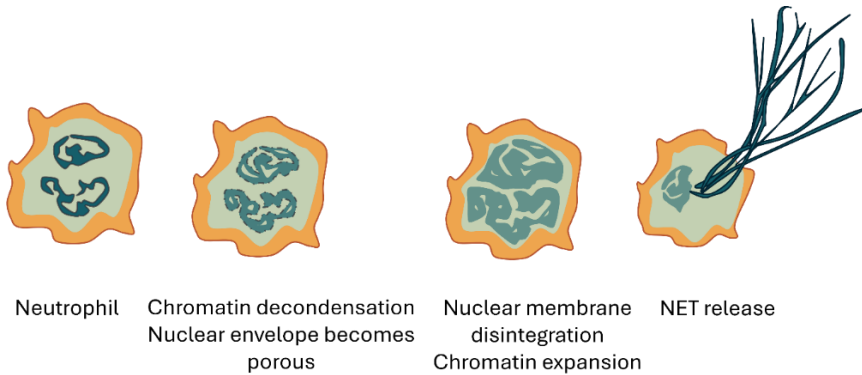


Figure 1: Schematic illustration of the four steps of the neutrophil extracellular trap formation process. From left to right a neutrophil in its resting state, the first steps of chromatin decondensation, The disintegration of the nuclear membrane, and finally the release of NETs.

NETs are formed as neutrophil DNA is uncoiled and released from within the cell membrane into the extracellular space where it acts as a trap for pathogens. The first paper on characterization of NETs was published by Brinkmann *et. al.* in 2004.¹⁴ NETs are composed mainly of DNA combined with histones, proteases, anti-microbial molecules and granule derived proteins. The NETs are also shown to contain primary granular proteins such as NE, cathepsin G and MPO. Lactoferrin and gelatinase, usually found in secondary and tertiary granules are also found as well as both nuclear and mitochondrial DNA.³⁶ Yousefi *et. al.* generated fibrous NETs in vitro with NETs containing only mitochondrial DNA, demonstrating an alternative composition.³⁷

NET formation can be divided into three stages³⁸:

- nuclear envelope disintegration/rupture
- nuclear chromatin decondensation
- plasma membrane rupture

Nuclear envelope disintegration/rupture:

The nuclear envelope consists of two lipid bilayers, the outer and the inner, inside of the inner membrane towards the nucleoplasm, a lamina mesh network help preserve the structural integrity of the envelope. There are two types of lamins present in the network, A/C forming thick filaments and B forming thin organized filaments. Rupture of the network occurs when lamin B is disassembled but not fragmented of the lamina.³⁹ Control of NET formation has also been observed to involve enzymes important for cell division by altering the A/C type.⁴⁰ These enzymes are mostly present in the cytoplasm, and it has been indicated that intact actin cytoskeleton may be required for the translocation of the enzymes into the nucleus.^{41,42} It has on the other hand been reported that the major physical force leading to envelope rupture is the chromatin swelling driven by decondensation.⁴³

Chromatin decondensation:

Inside the nucleus, DNA is tightly wrapped around histones. Histones are barrel like proteins with positive arginine groups that bind to the negative DNA. Winding the DNA around the histones form a complex called chromatin. From the histone core, tails of N-terminals present lysine protrude. Lysine is net positively charged but if acetylated by histone acetyltransferase (HAT) the positive charge can be replaced by an acetyl group. Acetylation may thus cause chromatin decondensation during NET formation, by loosening the attracting forces between histones and DNA.⁴⁴

Chromatin is classified as a tightly packed heterochromatin or loosely packed euchromatin. The enzyme peptidyl arginine deiminase type-4 (PAD4) may neutralize the positive arginine on the histone by converting it into the neutral citrulline, increasing the repelling forces along the negatively charged phosphate groups of the DNA backbone, hence playing an important part in chromatin decondensation for NETs.⁴⁵ Furthermore, neutrophil elastase (NE) and MPO released from primary granules and translocated to the nucleus may promote decondensation as NE cleave histone subunits (H4) and MPO enhance by promoting a relaxed state of the chromatin. Ongoing research aim to deduce synergy between NE and MPO.⁴⁶

The pore forming protein GSDMD may be cleaved by NE activating it, leading to the hypothesis of a feedback loop where activation of GSDMD by NE leads to pore formation, promoting further release of NE. Pore formation in the nuclear membrane enables translocation of NE which decondenses the chromatin.⁴⁷

Plasma membrane rupture:

The third step in the process of NET release includes rupture of the plasma membrane. Thiam *et al.* describes that that NET-release is initiated by the cytoskeleton via disassembly of actin filaments.⁴⁸ Following actin disassembly, micro-vesicles containing cytosolic content start budding from the plasma membrane. At the same time, parts of the cytoskeleton start to disassemble.⁴⁸ This is then followed by nuclear envelope disintegration and chromatin decondensation, plasma membrane rupture and ultimately DNA expulsion.

1.3 Neutrophils and Nanoparticles

The immune response of NETs can, when unregulated, promote disease in the human body, but under normal circumstances acts as one of the first lines of defense against pathogens. Under circumstances such as gout NETs aggregation can also help resolve inflammation.⁴⁹ The antibacterial properties of NETs have in recent years captured the attention of material scientists. The rationale of using NETs and mimicking materials is to provide new tools to combat drug-resistant bacterial infections and minimize the use of antibiotics. For example the self-assembly of DNA structures into networks incorporating copper nanoparticles as antibacterial agent.⁵⁰ Another example is the use of non-DNA based networks which has been enhanced with enzyme mimicking functionality to emulate NETs while not being sensitive to DNA-degradation.⁵¹ The degradation of a biomaterial can however be beneficial after its intended use. Other researchers have focused on the modulation of NETs formation through differently charged hydrogels, affecting how the neutrophils interact with a material in different ways, from repair to inflammation at different sites of the material e.g. an implant.⁵²

Magnetic nanoparticles have been used in a range of applications in the biomedical field, such as a contrast agent in magnetic resonance imaging (MRI), as a magnetic targeting drug delivery system controlled by a strong external magnetic field and released at e.g. a tumour site.^{5,53,54} The nanoparticles can also be used as heating elements for magnetic hyperthermia treatment by generating heat when exposed to an alternating magnetic field. This heat generating property is utilized for targeted cancer treatment, locally heating the tumor.⁴ Magnetic nanoparticles specifically binding to cells of interest also allow for separation and sorting of cells.^{55,56} The magnetic

properties of these nanoparticles are also being used as a means to emulate different environments to promote cell growth in 3D matrices such as hydrogels.⁵⁷⁻⁶⁰ A hydrogel consists of around 90% water and is often used to mimic the 3D structure inside the body. However, certain cell types may require dynamic or anisotropic environments.^{61,62} In the presence of a magnetic field, iron oxide nanoparticles can form nanochains, anisotropic structures with high aspect ratio and exhibit controlled directionality. Incorporation of such anisotropic structures into a hydrogel has been shown to promote the regeneration of nerve cells for repair of spinal cord injury.⁶³ Since the particles are still affected by a magnetic force while embedded in a hydrogel, the use of magnetic iron oxide nanorods have been shown to increase the stiffness of a hydrogel in order to emulate the dynamic mechanical milieu of real tissue.⁶⁴

In combination, recent NETs and nanoparticle research have provided insights such as capping strategies for modulated NETs response and as a hitchhiking strategy past the blood-brain/cord barrier.^{65,66} However, little have been researched about the possibilities of a combined NETs-magnetic iron oxide nanoparticle and their properties as a structural element for bio-architecture.

1.4 Photoemission

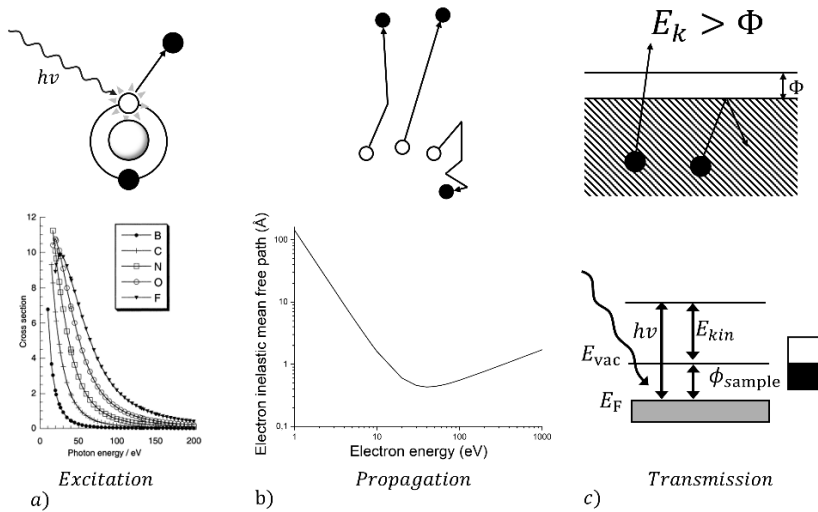


Figure 2: a) excitation of electron by absorption of a photon and an example of the photoionization cross-section, graph printed with permission from⁶⁷. b) propagating electrons showing from the left inelastic scattering, elastic scattering and multiple inelastic scattering events and the IMFP below. c) transmission occurs only when the work function is overcome.

In surface science, photoemission forms the basis of the surface-sensitive analytical technique known as photoelectron spectroscopy (PES). PES can be used to study the electronic structure, elemental composition, and chemical states of materials.⁶⁸⁻⁷⁶ Photoemission is the process in which electrons are emitted from a material after absorbing energy from electromagnetic radiation.⁷⁷ This phenomenon is described by the photoelectric effect, first explained by Einstein.⁷⁸ Photons with higher energy can eject more tightly bound electrons, i.e., electrons located closer to the atomic core. To emit core-level electrons, X-rays are typically used, while ultraviolet (UV) light is sufficient to emit valence electrons.

Once emitted, the electron retains any excess energy beyond that required to overcome the binding energy and the work function as kinetic energy provided that no inelastic scattering occurs. The electron's kinetic energy can then be measured, and its binding energy determined using the photoelectric-effect equation:

$$E_B = h\nu - E_k - \phi_{spectrometer} \quad Eq. (1)$$

Where E_b is the binding energy, $h\nu$ the absorbed photon energy, E_k the kinetic energy of the emitted electron and ϕ the spectrometer work function.

Photoelectron Spectroscopy (PES) has several experimental variants depending on the photon source, detection geometry, and the type of information sought. **Commonly used techniques include:**

1. **X-ray Photoelectron Spectroscopy (XPS):** Provides information on the elemental composition, chemical states, and electronic states of materials.
2. **Ultraviolet Photoelectron Spectroscopy (UPS):** Focuses on the valence band and molecular orbital structure of materials.
3. **Angle-Resolved Photoemission Spectroscopy (ARPES):** Measures the emission angles of the photoemitted electrons to map the electronic band structure.

1.4.1 Electron excitation

Electron excitation occurs when an electron absorbs energy and transitions to a higher energy state, thereby overcoming the attractive forces of the positively charged nucleus, as illustrated in Figure 2 a). In photoemission, photons provide this energy, which is absorbed by the electron, causing it to escape from the atom.

The likelihood of absorption depends on the element and the photon energy and is described by the photoionization cross-section $\sigma(\omega)$. This cross section is highest near the ionization threshold and decreases with increasing photon energy due to interference effects between the emitted electron wave and the remaining (vacated) orbital. The cross section depends on the spatial shape of the orbital. For example, when comparing the second period elements, carbon has a broader and a more radially extended 2p orbital than the more electronegative oxygen 2p orbital. As a result, the emitted electron wave from carbon interacts with the orbital for a longer time, leading to stronger interference effect and thus a faster decay of the cross section compared to oxygen⁶⁷. Consequently, XPS is more sensitive to elements with higher photoionization cross section.

1.4.2 Electron propagation

Once an electron has been excited and begins to propagate through the sample, it frequently interacts with the electrons and nuclei of other atoms. During transport through the solid, electrons may exchange energy and momentum through elastic (no energy loss) and inelastic (energy loss occurs) scattering processes, as illustrated in Figure 2 b). As the electrons travel through the material, longer paths increase the probability of inelastic scattering events, generating secondary electrons and reducing the kinetic energy by a significant fraction of the emitted electrons.

This process contributes to a background signal in the photoemission spectrum, which appears shifted towards lower kinetic energies. The average distance an electron travels between scattering events is known as the inelastic mean free path (IMFP). The IMFP depends on the electron's kinetic energy and is represented by the “**universal**

curve” which shows a broadly similar behaviour for all elements with larger IMFP values at both, low and high kinetic energies.⁷⁹

In the kinetic energy range of approximately 30-50 eV, electrons can efficiently excite plasmons, generate electron-hole pairs and induce vibrational excitations in chemical bonds leading to a minimum in the IMFP, as shown in Figure 2 b). At lower energies, these energy loss events are less likely due to insufficient energy to excite these processes, while at higher energies, faster transit of electrons through the solid reduces the probability of interaction⁸⁰.

For imaging and spectral analysis, a longer IMFP is desirable because it increases the detectable photoelectron intensity. This is described in equation 1:

$$I(l) = I_0 e^{-\frac{l}{\lambda_{in}}} \quad Eq. (2)$$

where:

- I is the intensity after traveling a distance l ,
- I_0 is the initial intensity of the electrons,
- l is the travel path, and
- λ_{in} is the IMFP.

1.4.3 Electron transmission

Electrons reaching the surface may either be reflected or transmitted, depending on their energy (see Figure 2c). The energy required for an electron to escape through the surface is the material’s work function Φ . If the electron’s energy exceeds this barrier, it can be emitted into the vacuum. By measuring the electron emission, the work function of the surface can be determined⁸⁰.

1.5 Work function

Work function is the minimum energy required for an electron in a solid to escape from its highest occupied state (the Fermi level), into the vacuum, such that it is no longer influenced by the solid. Near the surface of a material, the distribution of electrons does not end sharply at the atomic boundary. Instead, the electron density extends slightly beyond the surface by a few Ångströms. Because the electronic structure differs between materials, the extent of this extension also varies. This leads to a small “spill-out” of electron density into the region just outside the solid, creating a slightly negative charge immediately outside the surface. The negative charge is mirrored by an equally large positive charge just below the surface, resulting in a surface dipole due to the redistribution of electron density near the surface plane.

A larger spill-out generally results in a higher work function, as more energy is required for the electron to overcome the surface dipole. Surface geometry also influences this spill-out. More closely spaced atoms can increase the electron density available for spill-out. The work function of the bare surface is influenced by two factors: the electronic properties of the material and its surface dipole.

Adsorption onto the surface can alter the surface dipole layer. An electron-donating adsorbate increases the dipole and thereby raises the work function, while an electron-withdrawing adsorbate reduces the dipole and lowers the work function.

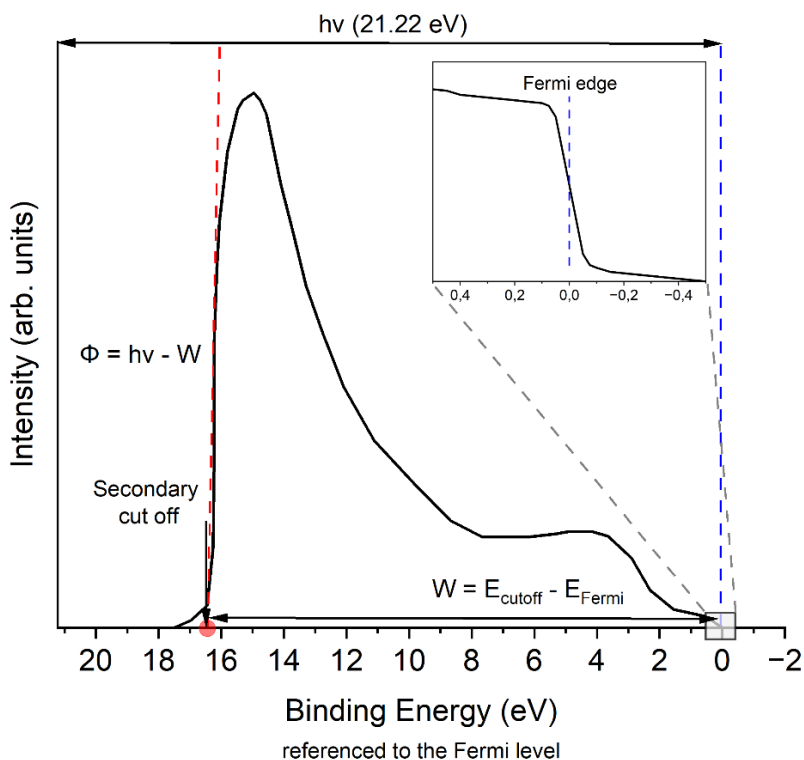


Figure 3: Photoemission spectrum illustration with a He I (21.22 eV) light source. The inset shows a close-up of the spectrum of the Fermi edge.

Excitation with a UV source such as a He I (21.22 eV) lamp is sufficient to emit the loosely bound valence electrons without ejecting core-level electrons. This range is ideal for determining the work function. Electrons excited from the Fermi level will have the highest kinetic energy, while electrons that barely overcome the work function, either due to being excited from lower levels or due to energy loss events discussed earlier, form a peak at lower kinetic energies. The endpoint of that peak is called the secondary cutoff.

To calculate the work function, the following equation is used:

$$\Phi = h\nu - W \quad \text{Eq. (3)}$$

where W is the width of the spectrum, calculated as the difference between the Fermi level and the secondary cutoff, see Figure 3. Given that the photon energy $h\nu$ is known, the work function Φ can be calculated.^{80,81}

Chapter 2

2 Methods

2.1 Neutrophil and NETs isolation

De-identified, non-traceable, whole blood samples from apparently healthy consenting donors were supplied by the blood bank at Linköping University hospital in Na-heparin tubes. Following analysis, samples were discarded.

2.1.1 Neutrophil Isolation

Na-heparin tubes were used. There are other anti-coagulants that has been shown to give a higher final yield of neutrophils but with the compromise of being less active⁸². The isolation is started as soon as possible due to the short lifespan of the neutrophils. The principle behind the neutrophil isolation is a density gradient media, for this thesis the media used is called PolymorphPrep™.

To determine the yielded concentration of neutrophils a Bürker chamber is used. The cell suspension can then be diluted into a desired concentration of e.g. 1×10^6 cells/ml in buffer.

The cells are then incubated on TL-1 washed silicon surfaces or on gridded/normal glass cover slips in well plates at 37C. To preserve the cell structure and stop the experiment paraformaldehyde(PFA) is added to a final concentration of 0.67%.

2.2.2 NETs Isolation

To induce NETs release, neutrophils are incubated together with phorbol myristate acetate (PMA), a PKC activator. If NETs are to be isolated PFA is not added. To isolate the NETs the buffer media is aspirated gently and discarded to get rid of any loosely bound cells. Any NETs on the surface are then rinsed off and collected into tubes and centrifuged at 4C. The pellet should now consist of cells and aggregated NETs, while any non-aggregated NETs should remain in the supernatant. The supernatant is further centrifuged once more and the final DNA concentration of the supernatant is then measured using a Qubit-fluorometer.

2.2 NanoESCA

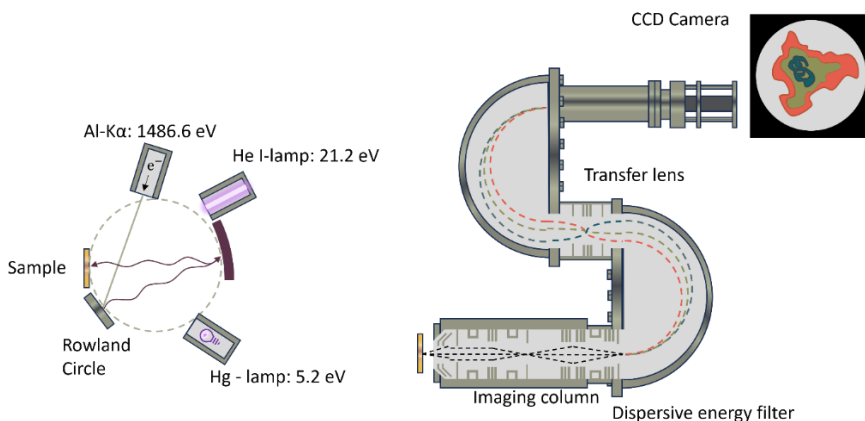


Figure 4: Schematic illustration of the NanoESCA instrument. Three different light sources can be used illustrated to the left. Electrons extracted from the surface are then imaged by an imaging column and passes through the IDEA system via a transfer lens and is finally imaged by a CCD camera. A neutrophil is illustrated as an example image with different regions appearing at different energies.

The PES techniques described in the previous chapter all build on the same principle of the photoelectric effect. It therefore makes sense to combine these similar techniques into a single instrument. The NanoESCA is primarily a microscopy instrument that combines imaging modalities X-ray Photoelectron Spectroscopy (XPS), Photoemission Electron Microscopy (PEEM/UPS), and Angle-Resolved Photoemission Spectroscopy (ARPES). The work in this thesis focuses on the first two techniques. The unique feature of the NanoESCA system illustrated in Figure 4 is that it has an imaging double energy analyzer (IDEA) positioned after an imaging column. It consists of two hemispherical analyzers oriented 180° towards each

other and connected via a transfer lens enabling spherical-aberration-corrected, energy-filtered image stacks.⁸³⁻⁸⁵

2.2.1 PEEM

Electron microscopy techniques rely on electromagnetic lenses whereas optical microscopy uses glass lenses and visible light to enable magnification and imaging. The foundational concepts of electron optics were outlined by H. Busch in 1926⁸⁶. In the early 1930s, two distinct approaches to physical electron optics merged: magnetic lenses studied by Knoll and Ruska, and electrostatic lenses explored by Brüche and Johannson. After imaging of an electron emitting cathode⁸⁷, Brüche and Johannson advanced the field by visualizing surfaces irradiated with ultraviolet light⁸⁸.

A significant contribution to the field of Photoemission Electron Microscopy (PEEM) was made in 1981 when Beamson et. Al. combined electron microscopy with an energy filter, producing images containing both spectral and position information⁸⁹. Since then, PEEM has become an invaluable tool for surface science, widely used in materials research to analyze the electronic properties of semiconductors, nanomaterials and grain boundaries of metals.

In 1971 Gertrude F Rempfer and O. Hayes Griffith pioneered the imaging of biological samples with PEEM by capturing sections of rat epididymis, viruses and microtubules.⁹⁰⁻¹⁰⁵ Rempfer also made significant contributions to the development of the PEEM lens system, further cementing her influence in the field.

The principle of PEEM involves the excitation and emission of surface electrons using UV light. The contrast is captured as local variations in work function. Photoemitted electrons are accelerated by an electric field of ~ 15 kV and extracted into an electrostatic objective lens, where initial magnification occurs.

The electrons are then separated based on their emission angle, with wider angles causing spherical aberration and reducing lateral resolution. To address this, a contrast aperture limits the accepted angles, improving image quality. Deflectors direct the electrons while stigmators correct lens asymmetries caused by small shape variations in the lens. Along with a transfer lens these elements create the first image plane.

Lenses filter out electrons with insufficient kinetic energy, allowing only those at a desired threshold to pass through. Electrons emitted at specified angles and energies are then magnified and imaged at a final image plane at the end of the PEEM column. This image is amplified by a multichannel plate, and projected onto a phosphor screen, converting the electrons into photons. The light is then transferred through optical fibers to a CCD camera for imaging.¹⁰⁶⁻¹⁰⁹

2.2.2 X-ray photoelectron spectroscopy

In the 1950's Kai Siegbahn and his research team in Uppsala developed a method to measure the binding energies of electrons emitted with high accuracy using the photoelectric effect.¹¹⁰ In 1981 he received the Nobel prize “for his contribution to the development of high-resolution electron spectroscopy”.¹¹¹ The technique is a cornerstone in materials science, surface science, and nanoscience and an invaluable tool for chemical composition analysis.

XPS is a surface sensitive technique, with 95% of the signal intensity coming from the topmost 10 nm. Core electrons are the electrons most affected by the nuclear charge and do not participate in bonding. Since heavier elements have more protons, the binding energy of those electrons is higher. To extract core electrons from the surface, an X-ray source is required. X-rays can be generated by bombarding a surface with high-kinetic-energy-electrons.^{112,113}

Heating a tip made of a low work function material such as lanthanum hexaboride yields an intense stream of electrons.¹¹⁴ These electrons are typically directed at an aluminum anode. The inner $K\alpha$ -shell electrons of the aluminum are excited by the incoming electrons but subsequently relax and release that energy in the form of photons. The characteristic emission energy of Al $K\alpha$ X-rays forms a sharp peak on the X-ray emission spectrum at 1486.7 eV which is suitable for use as an X-ray source.

Unfortunately, many electrons bend their trajectory due to the nuclear charge of aluminum, releasing photons. This process produces what is called bremsstrahlung, an unwanted form of X-rays in this case. A monochromator made from quartz crystal can filter out the bremsstrahlung by only reflecting light of a certain wavelength at a specific angle. The X-ray beam is focused on the sample by placing the monochromator on a Rowland circle and bending the crystal to a radius twice the radius of the Rowland circle, see Figure 4.

Photoemitted electrons are then collected via a lens system into a hemispherical analyzer, a device that filters electrons based on kinetic energy. A hemispherical analyzer separates electrons with different kinetic energy via an applied potential between an inner and outer hemisphere. Electrons with higher kinetic energy are less affected by the potential than those with lower energy, meaning they will turn in a wider orbit. Before entering the analyzer, the electrons are retarded

down to a selected pass energy E_{pass} , described by equation 4, and only electrons at the pass energy are able to pass through the analyzer:¹¹⁵

$$E_{pass} = e\Delta V \left(\frac{R_1 R_2}{R_1^2 - R_2^2} \right) \quad Eq. (4)$$

Where e is the electron's charge, ΔV is the potential difference between the two hemispheres, and R_1 and R_2 are the inner and outer radii. Since the radii are constant and depend on the design of the spectrometer, the equation is usually written as $E_{pass} = ke\Delta V$ where k is the spectrometer constant. An electron precisely at the pass energy will follow the equidistant plane between the two concentric hemispheres of the analyzer. A slit is situated after the analyzer, allowing only a narrow band of electrons with a certain energy to pass through. A channeltron then measures the intensity at the selected energy.¹¹⁵

XPS data is presented as a spectrum of binding energies, calculated from the measured kinetic energy. The area under a peak corresponds to the quantity of the element in the sample. Core electrons are affected indirectly by valence electrons that participate in bonding. The core electron of carbon will shift towards higher binding energies when the atom is bonded to a more electronegative atom such as oxygen. The shift of peaks helps determine the chemical environment of the atoms. From peak shifts and area, XPS can determine the chemical composition of surfaces with an accuracy of $\pm 10\%$ and can detect relative compositional changes of 1%.^{112,116-118}

2.2.3 Imaging XPS and energy filtered PEEM

To transform purely spectral data into images where each pixel contains spectral information two different acquisition approaches can be used: sequential and parallel.¹¹⁵

In sequential acquisition, the sample is scanned with the light beam in a raster pattern and a spectrum is recorded point by point. However, the lateral resolution of this method is limited by the size of the light spot and is typically on the order of a few micrometers.¹¹⁵

In parallel acquisition, an entire image is recorded at once while stepping through different energies. This approach is significantly faster and can produce images with a resolution on the order of tens of nanometers. This is the method used in this thesis. By recording a series of images over a range of energies, a stack of images is obtained in where the intensity variation across the energy dimension at each pixel forms a spectrum.¹¹⁵

There are three light sources on the NanoESCA system that enable measurements in three different energy ranges. To investigate the binding energies of core electrons, the Al K α X-ray source (1486.6 eV) is used. To study valence electrons, the He I (21.2 eV) lamp is employed. To measure the work function of electrons near the Fermi level, the Hg (5.2 eV) lamp is employed.

During imaging XPS measurements, the sample is grounded, and the energy scale is calibrated relative to the spectrometer's work function. To measure the work function with PEEM, the sample is instead placed under a negative bias to provide the electrons with sufficient energy to accelerate toward the objective lens.

Regardless of which light source is selected, the image is subsequently formed by the lens system in the PEEM column. In PEEM mode, at this stage one can choose either to use the IDEA system to obtain energy filtered PEEM or to bypass the IDEA system and instead filter out electrons with insufficient kinetic energy. In the latter case, the column effectively acts as a high-pass filter, where only areas of the sample with sufficiently low work function produce a signal.¹¹⁹ However, in this thesis only the energy-filtered mode has been used. After passing through the column, the electrons are directed into the first hemispherical analyzer. This energy filtering process introduces spherical aberration, meaning electrons with different energies are focused on different planes. To correct this a second hemispherical analyzer completes the orbit, making them coincide at their starting position i.e., all energies at the same plane regardless of kinetic energy or entry angle into the analyzer.⁸³⁻⁸⁵

2.3 Image Processing

For the energy-filtered methods, the result is obtained as a stack of images with energy along the z -axis in the format $I(x, y, E - E_F)$, where the energy is expressed relative to the Fermi level. This allows the stack to be scanned to extract an image at a specific energy level or to perform spectral analysis.

For imaging XPS and energy filtered PEEM, each pixel can be treated as an individual spectrum. By analyzing shifts in binding energy and variations in peak area or the local work function, information about the elemental composition, chemical environment and the surface's electronic properties can be obtained.¹¹⁹⁻¹²³

2.3.1 Work function (WF) mapping

The stack of images produced in energy filtered PEEM contains a series of images at the photoemission threshold ($E - E_F$) within a range in each pixel location (x, y). The local workfunction Φ of each pixel can be calculated into a 2D map by fitting a complementary error function to the rising side of the secondary electron peak as seen in equation 5 and Figure 5.

$$I(E - E_F) = \frac{I_{max}}{2} \operatorname{erfc} \left(\frac{\Phi - (E - E_F)}{\sigma\sqrt{2}} \right) + I_{off} \quad \text{Eq. (5)}$$

The height of the equation is set by the maximum intensity of the spectrum I_{max} divided by 2. σ is the standard deviation of the Gaussian which controls the slope of the sigmoid shape. This parameter is dependent on the slit width of the first hemisphere and the pass energy. The intensity offset I_{off} is calibrated towards the lowest intensity of the spectrum.^{124,125}

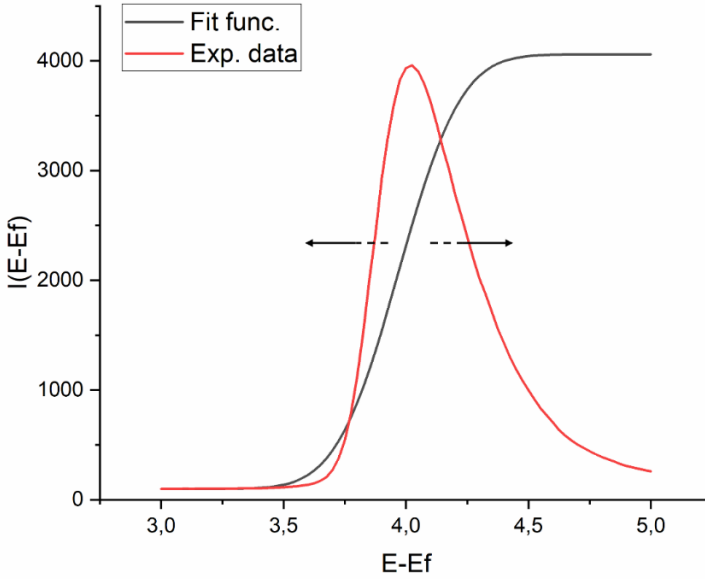


Figure 5: The complimentary error function used to fit the experimental data of a work function scan $E-E_f$. By fitting the error function to the left slope, the step of the secondary cut off can be measured and used to calculate the work function.

2.3.2 Non-isochromaticity

In energy filtered mode there is an energy shift across the y-axis of the image i.e., the axis of dispersion in the hemisphere.¹²⁶ This effect is attributed to electrons coming from off-axis points on the sample entering the hemisphere from the entrance lens at an angle.¹²⁷ The energy shift increases for larger pass energies. To correct for this artefact in each pixel column x_0 , the magnification at the first image plane M_1 and the focal length of the entrance lens f is used together with the pass energy in equation 6.

$$\Delta E = E_{pass} \left(\frac{M_1 x_0}{f} \right)^2 \quad \text{Eq. (6)}$$

2.3.3 Schottky effect

At an extraction voltage of 12kV under normal measuring conditions, the first extractor lens of the objective induces a strong electric field at the surface, i.e. the Schottky effect.¹²⁸ Using equation 7, the work function shift $\Delta E_{Schottky}$ can be calculated, where ϵ_0 is the vacuum permittivity ($8.854188 \times 10^{-12} \text{ F m}^{-1}$) and a normal E_{ext} of $6.66 \times 10^3 \text{ kV m}^{-1}$. A normal expected work function shift due to this effect is around 0.098 eV.

$$\Delta E_{Schottky} = -e \left(\frac{eE_{ext}}{4\pi\epsilon_0} \right)^{1/2} \quad Eq. (7)$$

2.3.4 4D work function (WF) mapping

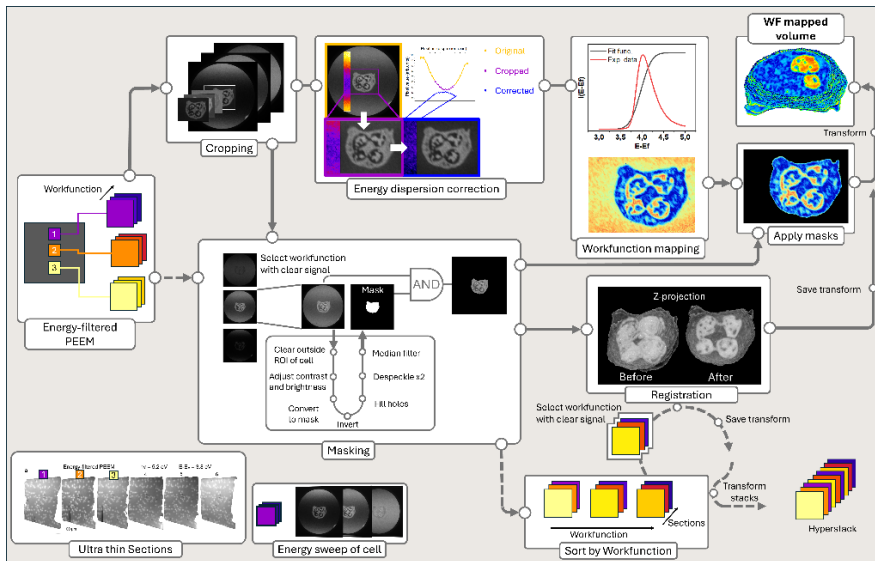


Figure 6: Overview of the processing steps to achieve a 4D work function mapped cell. Solid line pathways lead to a volumetric work function mapped cell, while dashed lines lead to a hyperstack used for sweeping through distinct energies $E-E_f$ of the cell volume.

The procedure to obtain a 4D volume of a cell begins by placing ultrathin sections sequentially on the SiO_x substrate, positioning them near the center of the surface to ensure optimal focusing conditions on the microscope. Acquisition starts by identifying the same cell on each section and using energy filtered PEEM to acquire an energy sweep stack, which forms the basis for the subsequent image processing steps.

Because of the geometry of the hemispherical energy analyzer, electrons entering the analyzer off-axis produce an energy dispersion along the y-direction of the image. This dispersion follows a second-order profile, meaning that the effect is strongest at the top and bottom of the field of view.¹²⁶ For this reason, it is important to position the

cell close to the center of the y-axis. To further reduce the influence of dispersion, the images are first cropped so that the stack contains a smaller region where the dispersion is less pronounced.

The cropped image stack is then subjected to dispersion correction. In this step, a region of uniform material, here the embedding resin is used as a reference to determine the dispersion profile. The correction algorithm considers all images in the stack and applies a transformation that flattens the dispersion curve across the entire dataset.

Following dispersion correction, a map of the local work function is generated using the full stack of images. This is achieved by fitting an error function as explained previously, to the spectrum obtained at each pixel location.¹²⁵

At the same time, the cropped stack is used for two additional tasks: generating masks that separate the cell from the surrounding resin and determining the transformations required for image registration. Mask creation begins by selecting an image at an energy where the contrast between the cell and the resin is strong, allowing a single mask to be applied to all images in the stack. A sequence of processing steps, summarized in the masking workflow, is then performed to produce a binary mask representing the cell region. This mask can be combined with the original images using a logical AND operation to generate masked images.

Once masked images have been produced for all slices, they are aligned using the SIFT-based plugin “Register Virtual Stack Slices” in Fiji (ImageJ), applying a rigid transformation.¹²⁹ The calculated transformations can be stored and subsequently applied to align the corresponding masked work function maps. The resulting aligned stack can then be visualized using a suitable 3D viewer. In this work,

the “Volume Viewer” plugin available in Fiji was employed for this purpose

2.4 Infrared reflection absorption spectroscopy (IRAS)

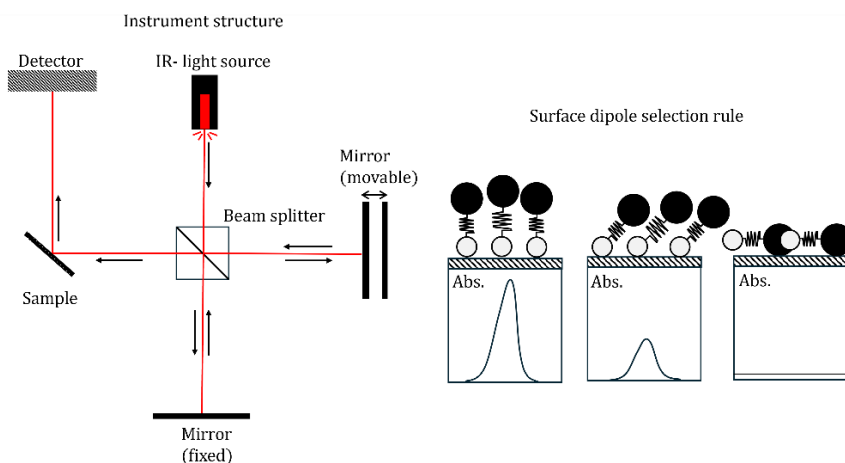


Figure 7: Structure of an IRAS instrument (left). Depiction of the surface dipole rule with resulting spectra (right).

Infrared Reflection Absorption Spectroscopy (IRAS) is a technique that uses infrared (IR) radiation to study the chemical bonds within a sample. It works by exposing the sample to a beam of IR radiation, which is absorbed by the sample at specific wavelengths that correspond to the vibrational frequencies of the chemical bonds in the sample. The absorption of IR radiation is then detected and recorded as an absorption spectrum, which is a graph that shows the intensity of the absorbed IR radiation as a function of the wavenumber of the bonds. Wavenumber is the number of wavelengths per unit distance and is often expressed in cm^{-1} .¹³⁰

The absorption spectrum is used to identify the chemical bonds present in the sample and to determine the structural and functional properties of the sample. IRAS is commonly used in a variety of fields, including

chemistry, biology, materials science, and environmental science, to study the composition and structure of molecules, to identify and quantify chemical compounds, and to determine the physical and chemical properties of materials.¹³¹⁻¹³⁴

The bond between two atoms can be described as two masses connected by a spring, a harmonic oscillator. The spring can be stretched and compressed requiring energy but on average it will be in its decompressed/unstretched state, which is the average bond distance. Compressing the spring further and further will require more and more energy as the positive nuclei repel each other. The spring can only be stretched so far until it breaks, separating the two masses. Taking this into consideration a Morse potential can be used, incorporating a bond dissociation energy limit. The math behind the harmonic oscillator is simpler than that of the Morse potential and since at lower temperatures, e.g., room temperature both models describe the bottom of the potential similarly well, the harmonic oscillator can be used to approximate the behaviour.¹³⁰

The energy levels of a bond are quantized meaning the levels occur in discrete steps by $\Delta E = hv$ (where h is Planck's constant and v is the vibrational frequency). The harmonic oscillator describes the frequency of a spring through the relation in equation 8,

$$v = \frac{1}{2\pi} \sqrt{\frac{k}{\mu}} \quad \text{Eq. (8)}$$

where k is the force constant and μ is the reduced mass of the two atoms in the bond in equation 9.¹³⁰

$$\mu[g] = \frac{m_1 m_2}{m_1 + m_2} \quad \text{Eq. (9)}$$

Converting the frequency from oscillations per second to oscillations per centimetre, the frequency is divided by the speed of light in centimetres $\bar{\nu} = \frac{\nu}{c}$.

The Morse potential in equation 10, uses an anharmonic approximation and better describes the repulsion between nuclei and the dissociation limit. In equation 10, v represents the vibrational quantum number and D the dissociation energy, i.e. the depth of the potential well.¹³⁵

$$E_v = h\nu \left(v + \frac{1}{2} \right) - \frac{h^2 \nu^2}{4D} \left(v + \frac{1}{2} \right)^2 \quad \text{Eq. (10)}$$

The masses of the atoms in the bond will not change, but the force constant will be different depending on the electronic conditions such as functional groups and its position in the molecule. Hence the information regarding a molecule's structure can be determined by IR-spectroscopy.

Fourier Transform Infrared Spectroscopy (FT-IR) is a type of infrared spectroscopy that uses a mathematical technique called Fourier Transform to analyze the absorbed IR radiation and convert it into an infrared spectrum. In FT-IR, the sample is exposed to a beam of IR radiation, and the resulting absorption spectrum is recorded as a function of time. The absorption spectrum is then analyzed using a mathematical algorithm namely the Fourier Transform, which converts the time-domain data into a frequency-domain spectrum. The resulting spectrum is called the Fourier Transform Infrared (FT-IR) spectrum, and it provides detailed information about the vibrational frequencies of the chemical bonds in the sample. All vibrations are not visible in the spectrum, the surface dipole selection rule states that the

only change in dipole moment of a vibrational mode is only IR-active if it oscillates perpendicular to the surface, see Figure 2 (right).

An FTIR instrument collects information from all infrared wavelengths simultaneously, only measuring the power of the light hitting the detector, see Figure 2(left). The power can be changed by using an interferometer. The resulting interference patterns hold information about all the wavelengths in that light simultaneously. In the interferometer light from a light source first hits a beam splitter which splits it into two separate perpendicular beams. The beams are reflected to the beam splitter by a set of mirrors positioned at equal distances. One beam is reflected again by the beam splitter toward a photodetector. The other is transmitted through the splitter. The beams are thus added up again before hitting the detector. Having one of the mirrors movable will result in one beam shifting in phase as the mirror moves. By changing the distance, altering the phase, different interference patterns are generated. If the light beams are completely in phase there will be maximum power reaches the detector, and if the beams are completely out of phase, there will be no power. Consequently, at every distance moved equal to half the wavelength the power signal will reach a minimum, and at each full wavelength moved will reach a maximum power. Calibrating the mirror position is performed by moving the mirror to a maximum and using it as a reference.¹³⁰

Signals with different wavenumbers appear as cosine waves which have been stretched out along the x-axis. The light source used in this instrument does not have a monochromator and thus many wavelengths i.e., wavenumbers, will be present in the light that hits the sample. Combining different cosine waves of different wavenumber will result in a signal which is very high in the beginning where all signals are still in phase i.e., start at the same point. As they end up more and more out of phase the combined signal will diminish as they cancel out i.e., the combined signal will ring out. This is the case for a signal combined from wavenumbers in successive order, but

when wavenumbers start being removed, the signal from the photodetector will deform and its ringing appearance will alter. The sample will act as a filter, absorbing photons of specific wavenumber, matching the vibrational modes of the sample. The missing wavenumbers can then be extracted from the interferogram using the Fourier transform. This creates a unique fingerprint of each sample. In conclusion the resulting IR spectrum is obtained by measuring the intensity of the transmitted (or reflected) radiation as a function of frequency (or wavenumber). The spectrum typically displays absorption bands, where each band corresponds to a specific vibrational mode that has absorbed energy.¹³⁰

Thus, the IR spectrum provides information about which vibrational modes are active in the sample, allowing the identification of functional groups and providing insights into the molecular structure.¹³⁶⁻¹⁴⁰

2.5 SEM

Scanning electron microscopy (SEM) is widely used in biological imaging because it provides much higher resolution than conventional optical microscopy. In SEM, a focused electron beam scans the sample surface in a raster pattern. Interactions between the electrons and the specimen generate signals, most commonly secondary electrons, which are detected to produce images reflecting surface morphology.¹⁴¹ Biological samples are often non-conductive and contain water, so they typically require fixation, dehydration, and coating with a thin conductive layer such as gold, platinum, or carbon to prevent charging. Low-vacuum or environmental SEM can reduce the need for coatings, allowing imaging of more delicate specimens.¹⁴² Secondary electrons are particularly sensitive to surface features, revealing detailed morphology. This makes SEM especially useful for studying cellular surfaces, tissues, microorganisms, and subcellular structures such as membranes or protrusions.^{143,144} With spatial resolution in the nanometer range, SEM enables investigation of micro- and nanoscale biological features that are sometimes inaccessible to light microscopy, making it a versatile tool for exploring the morphology, structure, and interactions of biological systems.

2.6 Fluorescence microscopy

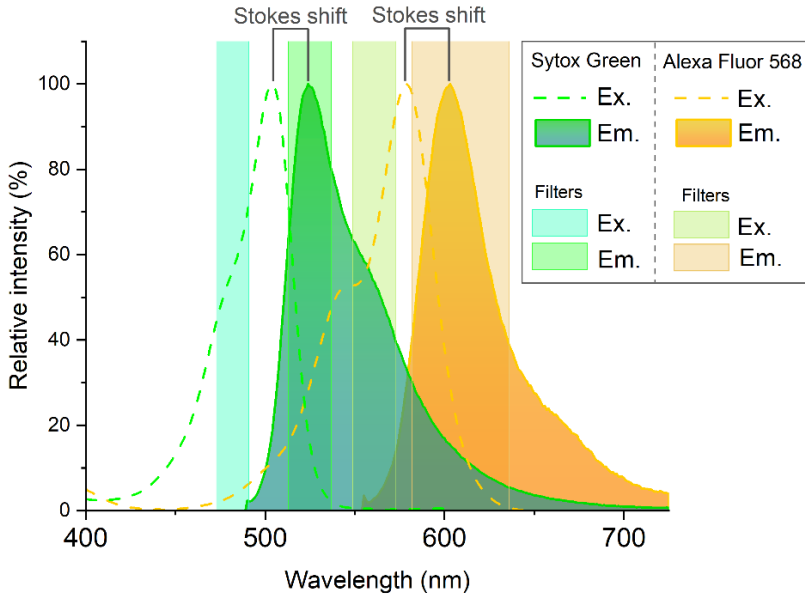


Figure 8: Fluorescence spectra of Sytox and Alexa Fluor 568 with corresponding Stokes shift. The filters used to the fluorophores are illustrated as bands.

2.6.1 Fluorescence

Fluorescence is the excitation of electrons by photons followed by emission of photons with a longer wavelength. The electron absorbs energy in the form of a photon, bringing it to an excited state. Electrons cannot, however, stay in these excited states indefinitely. The lifetime of excitation can be affected by e.g., interactions with other molecules, temperature or viscosity.¹⁴⁵⁻¹⁴⁷ As the electron relaxes down to a lower state, it releases energy in the form of a photon. The amount of energy,

emitted, depends on the energy difference between the excited state and the new state, where the ground state is the lowest. Typically, the emitted photon will have a lower energy than the absorbed and thus a lower wavelength. ^{148,149}

The size of a neutrophil is around 15 μ m which is about ten times smaller than the width of a human hair. To observe an individual cell and any subcellular content requires a microscope. But at this scale the cell is mostly translucent in visible light and organelles of the cell do not exhibit color. Fluorescent markers can help to visualize the cell structures. To use fluorescence we need a fluorophore, a molecule which converts light of one wavelength into another and emits it back. Fluorophores are generally combined with a moiety designed to prove the presence of a certain molecule, meaning their affinity often need to be highly specific. For some applications the fluorophore is coupled to an antibody which is the basis for immunohistochemistry.^{150,151} Others achieve high affinity by sheer molecular structure.¹⁵² A common fluorophore to image the DNA of cells is Sytox Green. In this thesis it has been used as a reporter for nuclear morphology and the presence of DNA. NETs consist mainly of DNA and are thus well suited to be imaged by Sytox Green.¹⁴ Sytox Green has two positive charges and is initially attracted to the negatively charged DNA by electrostatic attraction. When in close proximity to the DNA the molecule intercalates in between the base pairs of the DNA. This intercalation has been shown to increase the length of the DNA strand but without altering the mechanical properties. ¹⁵³

The fluorophore works by absorbing a photon supplied by the microscope's light source, which excites the fluorophore to a higher state. When the fluorophore relaxes back, the energy is released in the form of a photon with a lower energy due to energy losses.¹⁴⁹ The shift in wavelength from this process between absorption and emission is called the Stokes shift.¹⁵⁴ The process is not perfect in the sense that the wavelengths absorbed and emitted are not two discrete values. The caused broadening makes the use of multiple fluorophores more difficult, because the excitation band of one fluorophore may bleed into the absorption or excitation band of another as is illustrated in Figure 8.¹⁵⁵ When designing a fluorescence experiment it is therefore crucial to consider the stokes shift, band width and the distance in between the fluorophores' bands. In this thesis, the fluorophore Alexa Fluor568 coupled to phalloidin has been used to stain the cytoskeleton. Below, both fluorophores' spectral bands are plotted. We see that the emission band of Sytox Green is largely overlapping with the absorption band of Alexa 568. To solve this issue, the microscope is equipped with filters, filtering both the absorption and emission bands. Even though the Sytox Green band overlaps into the absorption band of the Alexa 568, the TRITC excitation filter will block the light that could excite the Sytox Green. Blocking the excitation also implies no emission. This process goes both ways, we see that the excitation filter of Aelxa568 starts right after the Absorption band of Sytox Green. Ultimately the goal is to optimize your setup to minimize any bleed through of signal into your bands for each fluorophore.

2.6.2 Structure of a microscope

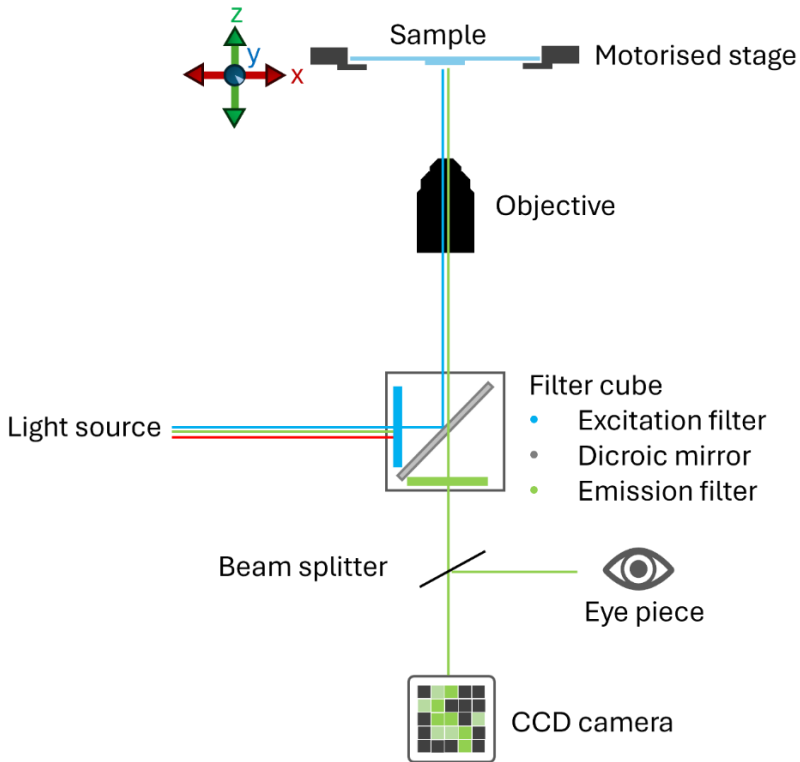


Figure 9: A schematic of the structure of a fluorescence microscope.

The structure of a conventional fluorescence microscope is as follows, and is illustrated in Figure 9. A light source produces a wide range of wavelengths. The light passes through a filter cube which houses the excitation filter, emission filter and a dichroic mirror. The excitation filter allows passage of the light with the wavelength needed to excite the fluorophores. The light is focused onto the sample by the objective, this is also where the magnification takes place. The fluorophores emit light with a longer wavelength which is again focused by the objective. The emission filter then only lets through the desired light and onto a CCD camera.¹⁰⁶ In between the excitation and emission filter sits a

dichroic mirror which will reflect the excitation light and let emission light pass. This further blocks any stray excitation light to pass through to the camera and is also used to direct the excitation light to the objective. A beam splitter is situated at the end to direct the light either to the eye piece or camera.¹⁴⁸ The sample is situated on a motorized stage able to move with sub- μm precision along 3 axes (x, y, z). Orientation around the sample is done via the x and y coordinates and to focus the sample it is moved in the z direction.

2.6.3 Measuring μ -Threads

In this thesis work I have used iron oxide nanoparticles together with NETs in order to make micro structures of these materials. Samples can have varied amounts of either magnetic field strength or iron oxide nanoparticles. To measure the length of NETs and Iron oxide nanoparticles one starts with an RGB image. As all the colors from a fluorescence microscope are artificial, we can convert the three-color channels to simple intensity by converting the image to 8-bit or similar. To get rid of some of the background noise and emphasize the threads the contrast and brightness is adjusted. By making the images binary we can use some convenient methods to calculate the length. Some of the longer threads will not be able to fit in the image and will thus have to be discarded from the measurement. We instruct the program to get rid of all threads that touches the border. Using a procedure called skeletonize each thread can be reduced to a single pixel wide line but keeping their full length except some end pixels.¹⁵⁶ These lines are very easy for the program to measure, resulting in a length/count distribution.

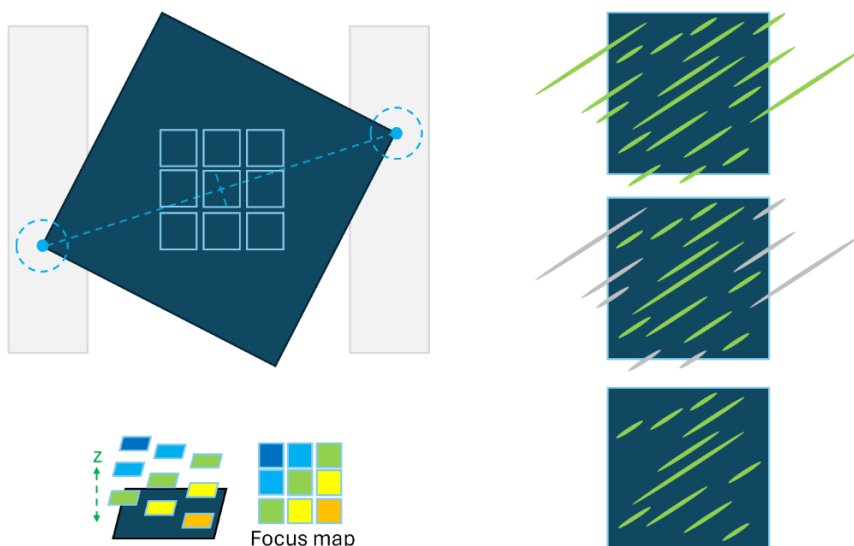


Figure 10: The procedure of acquiring a set of images in a repeatable manner over a larger area. Top left illustrates the calibration process of centering the microscope on the sample and the separation between acquisition points by a margin. Bottom left illustrates the focus map used to automate acquisition. To the right; an image showing nanoparticles and NETs μ -treads, with some threads outside the field of view. Going downwards threads touching the borders are removed and a filtered image is used for analysis.

The human eye is very good at being drawn to objects that are of interest to us, in microscopy this might lead to a subconscious biasing of information in images. To prevent such a bias when counting iron oxide NET threads so that samples are directly comparable to one another, we take the human out of the equation as much as possible. We do this by finding the centre of the sample and take a matrix of images at specified intervals. Typically, the samples would be placed at an angle over two double sided tape strips for easier transfer into a vacuum system, with less surface area being kept on the tape. To find the centre of the sample we can use the coordinates from the sample stage at two diagonally opposite corners and using the following equation 11:

$$X_c, Y_c = \frac{(X_1 + X_2)}{2}, \frac{(Y_1 + Y_2)}{2} \quad Eq. (11)$$

Where the left-hand side is the centre coordinates and the right-hand side the average of both corners. Once we have the centre of the sample, we can define the matrix so that each image is separated by some margin. There might be some tilt to the sample meaning focus need to be adjusted over sample. We can use the matrix coordinates and map the focus in the microscope's software. This focus map together with the matrix of coordinates create a method which is both scalable and enable image acquisition of many samples quickly.

Chapter 3

Summary of Papers

Paper I

Superparamagnetic Nanoparticle-Guided Alignment of Neutrophil Extracellular Traps

Andreas Skallberg, Filip Genander, Kalle Bunnfors, Caroline Brommesson and Kajsa Uvdal.

In manuscript

This study shows that iron oxide nanoparticles can be used to control the direction of neutrophil extracellular traps (NETs). Superparamagnetic nanoparticles were assembled into stable, wire-like structures via dipole–dipole interactions under a magnetic field and remained intact after field removal. We applied this approach to immune cells, with magnetic fields guiding the alignment of NETs during formation, as released NETs capture nanoparticles and align accordingly. The nanoparticles act as field-responsive elements, transferring magnetic forces to extracellular structures. This enables controlled spatial organization of NETs. Overall, magnetic self-assembly provides a strategy to direct immune-derived architectures, with potential applications in biomaterials, tissue engineering, regenerative medicine, and bio-inspired systems.

Paper II

Fabrication and characterization of Neutrophil extracellular traps- FeOx nanoparticle μ -threads

Filip Genander, Ida Hofvander, Andreas Skallberg, Caroline Brommesson and Kajsa Uvdal.

In manuscript

In this study, we demonstrate the characterization of, and the potential of, isolated neutrophil extracellular traps (NETs), combined with superparamagnetic iron oxide nanoparticles (SPIONs), can function as architectural building blocks. Under an applied magnetic field, NET–SPION assemblies form highly oriented, wire-like structures. By repeating the assembly process, multilayer configurations can be generated, enabling the creation of cross-patterned architectures. We further examine the relationship between structure length, SPION concentration, and magnetic field strength, observing a clear dependence that indicates the existence of an optimal parameter range. These findings establish NET–nanoparticle composites as a versatile platform for constructing organized, field-directed bio-structures.

Paper III

4D Work-Function Mapping of Neutrophil Subcellular Architecture

Filip Genander, Andreas Skallberg and Kajsa Uvdal.

In manuscript

In this work, we present a photoemission-based imaging approach that combines three-dimensional reconstruction with pixel-resolved work-function contrast to enhance cellular analysis. Using sequential ultrathin sections, we map the work-function (Φ) distribution in individual neutrophils and generate sub-micrometer volumetric reconstructions. This approach provides intrinsic electronic contrast across subcellular structures, including the plasma membrane, polymorphonuclear core, core membrane, and granule-rich cytoplasm. The work function at each pixel reflects the local elemental and chemical composition, adding an information layer beyond morphology. This method enables quantitative, cell-resolved surface-electronic characterization and highlights the potential of work-function mapping as a tool for biological imaging.

Paper IV

EGFR-Targeting Cerium–Gadolinium Core–Shell Nanoprobes for Imaging Head and Neck Squamous Cell Carcinoma

Anna du Rietz, Karin Roberg, Filip Genander, Per O.Å. Persson, Andreas Skallberg, Caroline Brommesson, Zhangjun Hu and Kajsa
Submitted to ACS OMEGA.

In this work, we developed epidermal growth factor receptor (EGFR)-targeting nanoprobes based on a core–shell architecture. The nanoparticles consist of a cerium oxide core doped with 3% gadolinium (Gd) and a poly acrylic acid (PAA) shell pre-functionalized with azide groups and the fluorophore FITC. Targeting specificity is introduced via conjugation of the monoclonal antibody cetuximab using click chemistry. The nanoprobes are systematically characterized with respect to core composition, shell functionalization, and antibody affinity. Finally, we demonstrate efficient and specific uptake in a head and neck squamous cell carcinoma cell line, confirming their potential for targeted cellular imaging.

Paper V

Coating and Functionalization of Multi Core Cerium–Gadolinium Oxide Nanoparticles via Plasma-Enhanced Chemical Vapor deposition

Anna du Rietz, Igor Zhirkov, Filip Genander, Alba Abeledo De La Vega, Clara Tran, Pierfrancesco Pagella, Andreas Skallberg, Caroline Brommesson, Marcela Bilek, Johanna Rosén, Kajsa Uvdal.

In manuscript

In this study, we investigated the formation of multi-core nanoparticles based on a previous formulation of cerium oxide and gadolinium. Multiple crystalline nanoparticles are integrated into a single particle by incorporation into an organic capping layer containing ketone functionalities, deposited via plasma-enhanced chemical vapor deposition (PE-CVD). The resulting structures are systematically characterized and subsequently functionalized through hydrazide coupling to the ketone groups, followed by azide–DBCO click chemistry for cetuximab conjugation. In addition, the impact of plasma treatment on the redox activity of cerium oxide is evaluated using X-ray photoelectron spectroscopy (XPS), providing insights into surface chemical modifications.

Chapter 4

Future Outlook

In this thesis, it was explored how work function can be used as a contrast mechanism for 3D rendered volumes of cells. introducing a fourth dimension, by adding electronic properties to cellular imaging. The area of PEEM in life science is still relatively unexplored and the outlook is interesting. Today, many microscopy techniques exist, and concepts can be borrowed from other fields. It would be interesting to investigate the use of techniques for deconvolution and super resolution. Just as in fluorescence microscopy, if the point spread function of the light source is known, images with even better contrast could possibly be achieved. Superresolution techniques appear to be a popular topic in literature on microscopy methods. Efforts have been made to make super-resolution methods that require only a standard computer and the intended microscope with the ability to acquire multiple (~100) images within a reasonable time frame. such methods could show potential for increasing resolution without the need for expensive hardware upgrades..

Another trend of the development of imaging or mapping techniques is the ability to distinguish between multiple cell types in histological samples. This could be a great area for PEEM as the spectral data could be used to train classifying models, not limited by structural features alone. Furthermore, the good contrast between elements in PEEM and imaging XPS could be utilized for the investigation of nanoparticle and cell interaction, even with a mixture of nanoparticles.

This thesis also explores the potential of iron oxide nanoparticles and NETs as a magnetically guided biomaterial. A natural step from this thesis would be to investigate the mechanical properties of these nanoparticle-NETs composites, it would also be needed to investigate the biocompatibility. These structures could also be incorporated into hydrogels to make materials responsive to magnetism while also contributing as a structural and biofunctional material. NETs also appears to be connected with microthrombi where platelets coagulate on NETs released in the bloodstream and adhere to endothelial walls in a directional manner. The structures developed in this thesis could provide a basis for controlled coverage and directionality of microthrombi models.

References

- 1 Neuwelt, A. *et al.* Iron-based superparamagnetic nanoparticle contrast agents for MRI of infection and inflammation. *AJR Am J Roentgenol* **204**, W302–313 (2015).
<https://doi.org/10.2214/ajr.14.12733>
- 2 Gupta, A. K. & Gupta, M. Synthesis and surface engineering of iron oxide nanoparticles for biomedical applications. *Biomaterials* **26**, 3995–4021 (2005).
<https://doi.org/https://doi.org/10.1016/j.biomaterials.2004.10.012>
- 3 Pankhurst, Q. A., Connolly, J., Jones, S. K. & Dobson, J. Applications of magnetic nanoparticles in biomedicine. *Journal of Physics D: Applied Physics* **36**, R167 (2003). <https://doi.org/10.1088/0022-3727/36/13/201>
- 4 Mai, B. T. *et al.* Thermoresponsive Iron Oxide Nanocubes for an Effective Clinical Translation of Magnetic Hyperthermia and Heat-Mediated Chemotherapy. *ACS Applied Materials & Interfaces* **11**, 5727–5739 (2019). <https://doi.org/10.1021/acsami.8b16226>
- 5 Liu, J. F., Jang, B., Issadore, D. & Tsourkas, A. Use of magnetic fields and nanoparticles to trigger drug release and improve tumor targeting. *WIREs Nanomedicine and Nanobiotechnology* **11**, e1571 (2019). <https://doi.org/https://doi.org/10.1002/wnan.1571>
- 6 Zhao, S., Yu, X., Qian, Y., Chen, W. & Shen, J. Multifunctional magnetic iron oxide nanoparticles: an advanced platform for cancer theranostics. *Theranostics* **10**, 6278–6309 (2020).
<https://doi.org/10.7150/thno.42564>
- 7 Zhao, Y., Zhao, X., Cheng, Y., Guo, X. & Yuan, W. Iron Oxide Nanoparticles-Based Vaccine Delivery for Cancer Treatment. *Molecular Pharmaceutics* **15**, 1791–1799 (2018).
<https://doi.org/10.1021/acs.molpharmaceut.7b01103>
- 8 Griffiths, D. J. & Schroeter, D. F. *Introduction to Quantum Mechanics*. 3 edn, (Cambridge University Press, 2018).
- 9 Kittel, C. *Introduction to solid state physics*. 8. ed. edn, 308-310, 323 -355 (Hoboken, N.J. Wiley, c2005, 2005).
- 10 in *Introduction to Magnetic Materials* 175–195 (2008).

- 11 Bean, C. P. & Livingston, J. D. Superparamagnetism. *Journal of Applied Physics* **30**, S120–S129 (1959).
<https://doi.org/10.1063/1.2185850>
- 12 Németh, T., Sperandio, M. & Mócsai, A. Neutrophils as emerging therapeutic targets. *Nature Reviews Drug Discovery* **19**, 253–275 (2020). <https://doi.org/10.1038/s41573-019-0054-z>
- 13 Burn, G. L., Foti, A., Marsman, G., Patel, D. F. & Zychlinsky, A. The Neutrophil. *Immunity* **54**, 1377–1391 (2021).
<https://doi.org/https://doi.org/10.1016/j.immuni.2021.06.006>
- 14 Brinkmann, V. *et al.* Neutrophil Extracellular Traps Kill Bacteria. *Science* **303**, 1532–1535 (2004).
- 15 Ehrlich, P.
- 16 Baggiolini, M., Bretz, U., Dewald, B. & Feigenson, M. E. The polymorphonuclear leukocyte. *Agents and Actions* **8**, 3–10 (1978).
<https://doi.org/10.1007/BF01972395>
- 17 Borregaard, N. & Cowland, J. B. Granules of the Human Neutrophilic Polymorphonuclear Leukocyte. *Blood* **89**, 3503–3521 (1997).
<https://doi.org/https://doi.org/10.1182/blood.V89.10.3503>
- 18 Carvalho, L. O., Aquino, E. N., Neves, A. C. D. & Fontes, W. The Neutrophil Nucleus and Its Role in Neutrophilic Function. *Journal of Cellular Biochemistry* **116**, 1831–1836 (2015).
<https://doi.org/https://doi.org/10.1002/jcb.25124>
- 19 Steven, J. L. Metchnikoff on the Comparative Pathology of Inflammation. *Glasgow Med J* **38**, 195–205 (1892).
- 20 Amulic, B., Cazalet, C., Hayes, G. L., Metzler, K. D. & Zychlinsky, A. Neutrophil Function: From Mechanisms to Disease. *Annual Review of Immunology* **30**, 459–489 (2012).
<https://doi.org/10.1146/annurev-immunol-020711-074942>
- 21 Tweedy, L. *et al.* Seeing around corners: Cells solve mazes and respond at a distance using attractant breakdown. *Science* **369**, eaay9792 (2020). <https://doi.org/10.1126/science.aay9792>
- 22 Roy, J., Mazzaferri, J., Filep, J. G. & Costantino, S. A Haptotaxis Assay for Neutrophils using Optical Patterning and a High-content Approach. *Scientific Reports* **7**, 2869 (2017).
<https://doi.org/10.1038/s41598-017-02993-6>
- 23 Ji, C. & Huang, Y. Durotaxis and negative durotaxis: where should cells go? *Communications Biology* **6**, 1169 (2023).
<https://doi.org/10.1038/s42003-023-05554-y>

- 24 Franke, K. & Gruler, H. Galvanotaxis of human granulocytes: electric field jump studies. *European Biophysics Journal* **18**, 334–346 (1990). <https://doi.org/10.1007/BF00196924>
- 25 Friedl, P. & Wolf, K. Plasticity of cell migration: a multiscale tuning model. *Journal of Cell Biology* **188**, 11–19 (2009). <https://doi.org/10.1083/jcb.200909003>
- 26 Aoun, L. *et al.* Amoeboid Swimming Is Propelled by Molecular Paddling in Lymphocytes. *Biophysical Journal* **119**, 1157–1177 (2020). <https://doi.org/https://doi.org/10.1016/j.bpj.2020.07.033>
- 27 Chung, W.-L. *et al.* A network of mixed actin polarity in the leading edge of spreading cells. *Communications Biology* **5**, 1338 (2022). <https://doi.org/10.1038/s42003-022-04288-7>
- 28 Michael, M. & Parsons, M. New perspectives on integrin-dependent adhesions. *Current Opinion in Cell Biology* **63**, 31–37 (2020). <https://doi.org/https://doi.org/10.1016/j.ceb.2019.12.008>
- 29 Yoshida, K. & Soldati, T. Dissection of amoeboid movement into two mechanically distinct modes. *Journal of Cell Science* **119**, 3833–3844 (2006). <https://doi.org/10.1242/jcs.03152>
- 30 Inturi, S. *et al.* Modulatory Role of Surface Coating of Superparamagnetic Iron Oxide Nanoworms in Complement Opsonization and Leukocyte Uptake. *ACS Nano* **9**, 10758–10768 (2015). <https://doi.org/10.1021/acsnano.5b05061>
- 31 Warnatsch, A. *et al.* Reactive Oxygen Species Localization Programs Inflammation to Clear Microbes of Different Size. *Immunity* **46**, 421–432 (2017). <https://doi.org/https://doi.org/10.1016/j.immuni.2017.02.013>
- 32 Segal, A. W. HOW NEUTROPHILS KILL MICROBES. *Annual Review of Immunology* **23**, 197–223 (2005). <https://doi.org/https://doi.org/10.1146/annurev.immunol.23.021704.115653>
- 33 Witko-Sarsat, V., Rieu, P., Descamps-Latscha, B., Lesavre, P. & Halbwachs-Mecarelli, L. Neutrophils: Molecules, Functions and Pathophysiological Aspects. *Laboratory Investigation* **80**, 617–653 (2000). <https://doi.org/10.1038/labinvest.3780067>
- 34 Sengeløv, H., Kjeldsen, L., Diamond, M. S., Springer, T. A. & Borregaard, N. Subcellular localization and dynamics of Mac-1 (alpha m beta 2) in human neutrophils. *The Journal of Clinical Investigation* **92**, 1467–1476 (1993). <https://doi.org/10.1172/JCI116724>

- 35 Faurischou, M. & Borregaard, N. Neutrophil granules and secretory vesicles in inflammation. *Microbes and Infection* **5**, 1317–1327 (2003).
<https://doi.org/https://doi.org/10.1016/j.micinf.2003.09.008>
- 36 Boeltz, S. *et al.* To NET or not to NET: current opinions and state of the science regarding the formation of neutrophil extracellular traps. *Cell Death & Differentiation* **26**, 395–408 (2019).
<https://doi.org/10.1038/s41418-018-0261-x>
- 37 Yousefi, S., Mihalache, C., Kozłowski, E., Schmid, I. & Simon, H. U. Viable neutrophils release mitochondrial DNA to form neutrophil extracellular traps. *Cell Death & Differentiation* **16**, 1438–1444 (2009). <https://doi.org/10.1038/cdd.2009.96>
- 38 Liu, M.-L., Lyu, X. & Werth, V. P. Recent progress in the mechanistic understanding of NET formation in neutrophils. *The FEBS Journal* **289**, 3954–3966 (2022).
<https://doi.org/https://doi.org/10.1111/febs.16036>
- 39 Li, Y. *et al.* Nuclear envelope rupture and NET formation is driven by PKC α -mediated lamin B disassembly. *The EMBO Reports* **21**, EMBR201948779 (2020).
<https://doi.org/10.15252/embr.201948779>
- 40 Amulic, B. *et al.* Cell-Cycle Proteins Control Production of Neutrophil Extracellular Traps. *Developmental Cell* **43**, 449–462.e445 (2017).
<https://doi.org/https://doi.org/10.1016/j.devcel.2017.10.013>
- 41 Schmalz, D., Kalkbrenner, F., Hucho, F. & Buchner, K. Transport of protein kinase C α into the nucleus requires intact cytoskeleton while the transport of a protein containing a canonical nuclear localization signal does not. *Journal of Cell Science* **109**, 2401–2406 (1996). <https://doi.org/10.1242/jcs.109.9.2401>
- 42 Liu, M.-L. Functional actin cytoskeleton is required in early stage of NETosis induction. *Proceedings of the National Academy of Sciences* **117**, 22653–22654 (2020).
<https://doi.org/10.1073/pnas.2013790117>
- 43 Neubert, E. *et al.* Chromatin swelling drives neutrophil extracellular trap release. *Nature Communications* **9**, 3767 (2018).
<https://doi.org/10.1038/s41467-018-06263-5>
- 44 Hamam, H. J., Khan, M. A. & Palaniyar, N. Histone Acetylation Promotes Neutrophil Extracellular Trap Formation. *Biomolecules* **9**, 32 (2019).

- 45 Wang, Y. *et al.* Histone hypercitrullination mediates chromatin decondensation and neutrophil extracellular trap formation. *Journal of Cell Biology* **184**, 205–213 (2009). <https://doi.org/10.1083/jcb.200806072>
- 46 Papayannopoulos, V., Metzler, K. D., Hakkim, A. & Zychlinsky, A. Neutrophil elastase and myeloperoxidase regulate the formation of neutrophil extracellular traps. *Journal of Cell Biology* **191**, 677–691 (2010). <https://doi.org/10.1083/jcb.201006052>
- 47 Sollberger, G. *et al.* Gasdermin D plays a vital role in the generation of neutrophil extracellular traps. *Science Immunology* **3**, eaar6689 (2018). <https://doi.org/doi:10.1126/sciimmunol.aar6689>
- 48 Thiam, H. R. *et al.* NETosis proceeds by cytoskeleton and endomembrane disassembly and PAD4-mediated chromatin decondensation and nuclear envelope rupture. *Proceedings of the National Academy of Sciences* **117**, 7326–7337 (2020). <https://doi.org/doi:10.1073/pnas.1909546117>
- 49 Schauer, C. *et al.* Aggregated neutrophil extracellular traps limit inflammation by degrading cytokines and chemokines. *Nature Medicine* **20**, 511–517 (2014). <https://doi.org/10.1038/nm.3547>
- 50 Zhang, P. *et al.* Biomimetic Synthesis of Nanomachine Inspired from Neutrophil Extracellular Traps for Multimodal Antibacterial Application. *ACS Nano* **19**, 13202–13219 (2025). <https://doi.org/10.1021/acsnano.4c18948>
- 51 Wang, C. *et al.* Neutrophil Extracellular Traps-Inspired Hydrogen-Bonded Organic Framework-Based Bio-orthogonal Nanozymes for Enhanced Bacterial Capture and Sterilization. *ACS Applied Materials & Interfaces* **17**, 47396–47411 (2025). <https://doi.org/10.1021/acsmi.5c11332>
- 52 Lopez-Silva, T. L., Anderson, C. F. & Schneider, J. P. Modulating Neutrophil Extracellular Trap Formation In Vivo with Locoregional Precision Using Differently Charged Self-Assembled Hydrogels. *ACS Central Science* **11**, 465–478 (2025). <https://doi.org/10.1021/acscentsci.4c02198>
- 53 Ahrén, M. *et al.* A simple polyol-free synthesis route to Gd₂O₃ nanoparticles for MRI applications: an experimental and theoretical study. *Journal of Nanoparticle Research* **14**, 1006 (2012). <https://doi.org/10.1007/s11051-012-1006-2>
- 54 Xu, X. *et al.* Doping engineering of iron oxide nanoparticles towards high performance and biocompatible T1-weighted MRI

- contrast agents. *Rare Metals* **43**, 298–308 (2024).
<https://doi.org/10.1007/s12598-023-02443-5>
- 55 Myklatun, A., Cappetta, M., Winklhofer, M., Ntziachristos, V. & Westmeyer, G. G. Microfluidic sorting of intrinsically magnetic cells under visual control. *Scientific Reports* **7**, 6942 (2017).
<https://doi.org/10.1038/s41598-017-06946-x>
- 56 Gwon, K. *et al.* Designing magnetic microcapsules for cultivation and differentiation of stem cell spheroids. *Microsystems & Nanoengineering* **10**, 127 (2024). <https://doi.org/10.1038/s41378-024-00747-9>
- 57 Shi, Y., Li, Y. & Coradin, T. Magnetically-oriented type I collagen-SiO₂@Fe₃O₄ rods composite hydrogels tuning skin cell growth. *Colloids and Surfaces B: Biointerfaces* **185**, 110597 (2020).
<https://doi.org/https://doi.org/10.1016/j.colsurfb.2019.110597>
- 58 Du, V. *et al.* A 3D magnetic tissue stretcher for remote mechanical control of embryonic stem cell differentiation. *Nature Communications* **8**, 400 (2017). <https://doi.org/10.1038/s41467-017-00543-2>
- 59 Wang, X. *et al.* 3D-printed tissue repair patch combining mechanical support and magnetism for controlled skeletal muscle regeneration. *Bio-Design and Manufacturing* **5**, 249–264 (2022).
<https://doi.org/10.1007/s42242-021-00180-1>
- 60 Chen, W., Zhang, Z. & Kouwer, P. H. J. Magnetically Driven Hierarchical Alignment in Biomimetic Fibrous Hydrogels. *Small* **18**, 2203033 (2022).
<https://doi.org/https://doi.org/10.1002/smll.202203033>
- 61 Dickinson, R. B., Guido, S. & Tranquillo, R. T. Biased cell migration of fibroblasts exhibiting contact guidance in oriented collagen gels. *Annals of Biomedical Engineering* **22**, 342–356 (1994).
<https://doi.org/10.1007/BF02368241>
- 62 Tang, S. *et al.* Nanocomposite magnetic hydrogel with dual anisotropic properties induces osteogenesis through the NOTCH-dependent pathways. *NPG Asia Materials* **16**, 16 (2024).
<https://doi.org/10.1038/s41427-024-00535-x>
- 63 Hu, Y. *et al.* Magnetic nanochain-induced anisotropic nerve assembly for spinal cord injury repair. *Chemical Engineering Journal* **501**, 157681 (2024).
<https://doi.org/https://doi.org/10.1016/j.cej.2024.157681>

- 64 Chen, W., Zhang, Y., Kumari, J., Engelkamp, H. & Kouwer, P. H. J. Magnetic Stiffening in 3D Cell Culture Matrices. *Nano Letters* **21**, 6740–6747 (2021). <https://doi.org/10.1021/acs.nanolett.1c00371>
- 65 Raghavan, P. *et al.* Physicochemical Design of Nanoparticles to Interface with and Degrade Neutrophil Extracellular Traps. *ACS Applied Materials & Interfaces* **17**, 8862–8874 (2025). <https://doi.org/10.1021/acsami.4c17324>
- 66 Wu, Y. *et al.* NET formation-mediated in situ protein delivery to the inflamed central nervous system. *Nature Communications* **15**, 10747 (2024). <https://doi.org/10.1038/s41467-024-54817-7>
- 67 Green, J. C. & Decleva, P. Photoionization cross-sections: a guide to electronic structure. *Coordination Chemistry Reviews* **249**, 209–228 (2005). <https://doi.org/https://doi.org/10.1016/j.ccr.2004.02.012>
- 68 Eriksson, P. *et al.* Cerium oxide nanoparticles with antioxidant capabilities and gadolinium integration for MRI contrast enhancement. *Scientific Reports* **8**, 6999 (2018). <https://doi.org/10.1038/s41598-018-25390-z>
- 69 Selegård, L. *et al.* Biotinylation of ZnO Nanoparticles and Thin Films: A Two-Step Surface Functionalization Study. *ACS Applied Materials & Interfaces* **2**, 2128–2135 (2010). <https://doi.org/10.1021/am100374z>
- 70 Copie, O. *et al.* Adsorbate Screening of Surface Charge of Microscopic Ferroelectric Domains in Sol–Gel PbZr_{0.2}Ti_{0.8}O₃ Thin Films. *ACS Applied Materials & Interfaces* **9**, 29311–29317 (2017). <https://doi.org/10.1021/acsami.7b08925>
- 71 Hjort, M. *et al.* Surface Chemistry, Structure, and Electronic Properties from Microns to the Atomic Scale of Axially Doped Semiconductor Nanowires. *ACS Nano* **6**, 9679–9689 (2012). <https://doi.org/10.1021/nn303107g>
- 72 Guo, H. *et al.* Enabling Photoemission Electron Microscopy in Liquids via Graphene-Capped Microchannel Arrays. *Nano Letters* **17**, 1034–1041 (2017). <https://doi.org/10.1021/acs.nanolett.6b04460>
- 73 Leung, B. O., Hitchcock, A. P., Brash, J. L., Scholl, A. & Doran, A. Phase Segregation in Polystyrene–Polylactide Blends. *Macromolecules* **42**, 1679–1684 (2009). <https://doi.org/10.1021/ma802176b>
- 74 Leung, B. O., Hitchcock, A. P., Brash, J. L., Scholl, A. & Doran, A. An X-ray Spectromicroscopy Study of Protein Adsorption to

- Polystyrene–Poly(ethylene oxide) Blends. *Langmuir* **26**, 14759–14765 (2010). <https://doi.org/10.1021/la102432g>
- 75 Neff, A., Niefind, F., Abel, B., Mannsfeld, S. C. B. & Siefertmann, K. R. Imaging Nanoscale Morphology of Semiconducting Polymer Films with Photoemission Electron Microscopy. *Advanced Materials* **29**, 1701012 (2017).
<https://doi.org/https://doi.org/10.1002/adma.201701012>
- 76 Niefind, F., Neff, A., Mannsfeld, S. C. B., Kahnt, A. & Abel, B. Computational analysis of the orientation persistence length of the polymer chain orientation. *Physical Chemistry Chemical Physics* **21**, 21464–21472 (2019).
<https://doi.org/10.1039/C9CP02944C>
- 77 Berglund, C. N. & Spicer, W. E. Photoemission Studies of Copper and Silver: Theory. *Physical Review* **136**, A1030–A1044 (1964).
<https://doi.org/10.1103/PhysRev.136.A1030>
- 78 Einstein, A. Über einen die Erzeugung und Verwandlung des Lichtes betreffenden heuristischen Gesichtspunkt. *Annalen der Physik* **322**, 132–148 (1905).
<https://doi.org/https://doi.org/10.1002/andp.19053220607>
- 79 Seah, M. P. & Dench, W. A. Quantitative electron spectroscopy of surfaces: A standard data base for electron inelastic mean free paths in solids. *Surface and Interface Analysis* **1**, 2–11 (1979).
<https://doi.org/https://doi.org/10.1002/sia.740010103>
- 80 Attard, G. & Barnes, C. *Spectroscopic techniques for probing solid surfaces*. (Oxford University Press, 1998).
- 81 Whitten, J. E. Ultraviolet photoelectron spectroscopy: Practical aspects and best practices. *Applied Surface Science Advances* **13**, 100384 (2023).
<https://doi.org/https://doi.org/10.1016/j.apsadv.2023.100384>
- 82 Freitas, M., Porto, G., Lima, J. L. F. C. & Fernandes, E. Isolation and activation of human neutrophils in vitro. The importance of the anticoagulant used during blood collection. *Clinical Biochemistry* **41**, 570–575 (2008).
<https://doi.org/https://doi.org/10.1016/j.clinbiochem.2007.12.021>
- 83 Escher, M. *et al.* NanoESCA: a novel energy filter for imaging x-ray photoemission spectroscopy. *Journal of Physics: Condensed Matter* **17**, S1329 (2005). <https://doi.org/10.1088/0953-8984/17/16/004>

- 84 Escher, M., Winkler, K., Renault, O. & Barrett, N. Applications of high lateral and energy resolution imaging XPS with a double hemispherical analyser based spectromicroscope. *Journal of Electron Spectroscopy and Related Phenomena* **178-179**, 303–316 (2010).
<https://doi.org/https://doi.org/10.1016/j.elspec.2009.06.001>
- 85 Escher, M. *et al.* NanoESCA: imaging UPS and XPS with high energy resolution. *Journal of Electron Spectroscopy and Related Phenomena* **144-147**, 1179–1182 (2005).
<https://doi.org/https://doi.org/10.1016/j.elspec.2005.01.250>
- 86 Busch, H. Berechnung der Bahn von Kathodenstrahlen im axialsymmetrischen elektromagnetischen Felde. *Annalen der Physik* **386**, 974–993 (1926).
<https://doi.org/10.1002/andp.19263862507>
- 87 Brüche, E. & Johannson, H. Elektronenoptik und Elektronenmikroskop. *Naturwissenschaften* **20**, 353–358 (1932).
<https://doi.org/10.1007/BF01504926>
- 88 Brüche, E. Elektronenmikroskopische Abbildung mit lichtelektrischen Elektronen. *Zeitschrift für Physik* **86**, 448–450 (1933). <https://doi.org/10.1007/BF01341360>
- 89 Beamson, G., Porter, H. Q. & Turner, D. W. Photoelectron spectromicroscopy. *Nature* **290**, 556–561 (1981).
<https://doi.org/10.1038/290556a0>
- 90 Griffith, O. H. *et al.* Photoelectron Microscopy: A New Approach to Mapping Organic and Biological Surfaces. *Proceedings of the National Academy of Sciences* **69**, 561–565 (1972).
<https://doi.org/doi:10.1073/pnas.69.3.561>
- 91 Birrell, G. B., Habliston, D. L. & Griffith, O. H. Photoelectron imaging of viruses and DNA: evaluation of substrates by unidirectional low angle shadowing and photoemission current measurements. *Biophysical Journal* **67**, 2041–2047 (1994).
[https://doi.org/https://doi.org/10.1016/S0006-3495\(94\)80687-3](https://doi.org/https://doi.org/10.1016/S0006-3495(94)80687-3)
- 92 Birrell, G. B., Habliston, D. L., Hedberg, K. K. & Griffith, O. H. Silver-enhanced colloidal gold as a cell surface marker for photoelectron microscopy. *Journal of Histochemistry & Cytochemistry* **34**, 339–345 (1986). <https://doi.org/10.1177/34.3.3950384>
- 93 Birrell, G. B., Habliston, D. L., Nadakavukaren, K. K. & Griffith, O. H. Immunophotoelectron microscopy: the electron optical analog of immunofluorescence microscopy. *Proceedings of the National*

- Academy of Sciences* **82**, 109–113 (1985).
<https://doi.org/doi:10.1073/pnas.82.1.109>
- 94 Bruce Birrell, G., Hedberg, K. K., Habliston, D. L. & Griffith, O. H. Biological applications of photoelectron imaging: a practical perspective. *Ultramicroscopy* **36**, 235–251 (1991).
[https://doi.org/https://doi.org/10.1016/0304-3991\(91\)90153-W](https://doi.org/https://doi.org/10.1016/0304-3991(91)90153-W)
- 95 Griffith, O. H., Habliston, D. L., Birrell, G. B. & Schabtach, E. Photoelectron imaging of DNA. *Biopolymers* **29**, 1491–1493 (1990). <https://doi.org/https://doi.org/10.1002/bip.360291015>
- 96 Griffith, O. H., Habliston, D. L., Birrell, G. B. & Skoczylas, W. P. On the possibility of obtaining a physical map of genomes by photoelectron imaging. *Biophysical Journal* **57**, 935–941 (1990).
[https://doi.org/https://doi.org/10.1016/S0006-3495\(90\)82613-8](https://doi.org/https://doi.org/10.1016/S0006-3495(90)82613-8)
- 97 Griffith, O. H., Habliston, D. L., Birrell, G. B., Skoczylas, W. P. & Hedberg, K. K. Biological photocathodes: Complexes of chlorophylls and hemes examined by photoelectron microscopy. *Proceedings, annual meeting, Electron Microscopy Society of America* **47**, 1056–1057 (1989).
<https://doi.org/10.1017/S0424820100157267>
- 98 Griffith, O. H., Habliston, D. L., Birrell, G. B., Skoczylas, W. P. & Hedberg, K. K. Biological photocathodes. *Proceedings of the National Academy of Sciences* **86**, 1826–1830 (1989).
<https://doi.org/doi:10.1073/pnas.86.6.1826>
- 99 Griffith, O. H., Hedberg, K. K., Desloge, D. & Rempfer, G. F. Low-energy electron microscopy (LEEM) and mirror electron microscopy (MEM) of biological specimens: Preliminary results with a novel beam separating system. *Journal of Microscopy* **168**, 249–258 (1992). <https://doi.org/https://doi.org/10.1111/j.1365-2818.1992.tb03267.x>
- 100 Griffith, O. H. & Rempfer, G. F. Photoelectron imaging and photoelectron labeling. *Ultramicroscopy* **24**, 299–312 (1988).
[https://doi.org/https://doi.org/10.1016/0304-3991\(88\)90317-8](https://doi.org/https://doi.org/10.1016/0304-3991(88)90317-8)
- 101 Habliston, D. L., Birrell, G. B., Griffith, O. H. & Rempfer, G. F. Photoelectron imaging of DNA: a study of substrates and contrast. *The Journal of Physical Chemistry* **97**, 3022–3027 (1993).
<https://doi.org/10.1021/j100114a032>
- 102 Habliston, D. L., Hedberg, K. K., Birrell, G. B., Rempfer, G. F. & Griffith, O. H. Photoelectron imaging of cells: photoconductivity extends the range of applicability. *Biophysical Journal* **69**, 1615–

- 1624 (1995). [https://doi.org/https://doi.org/10.1016/S0006-3495\(95\)80034-2](https://doi.org/https://doi.org/10.1016/S0006-3495(95)80034-2)
- 103 HEDBERG, K. K. & GRIFFITH, O. H. Immunophotoelectron Microscopy of the Cell Surface and Cytoskeletona. *Annals of the New York Academy of Sciences* **483**, 372–386 (1986).
<https://doi.org/https://doi.org/10.1111/j.1749-6632.1986.tb34545.x>
- 104 Houle, W. A. & Griffith, O. H. Photoelectron microscopy of viruses. *Ultramicroscopy* **11**, 71–74 (1983).
[https://doi.org/https://doi.org/10.1016/0304-3991\(83\)90056-6](https://doi.org/https://doi.org/10.1016/0304-3991(83)90056-6)
- 105 Nadakavukaren, K. K. & Griffith, O. H. Photoelectron imaging of cytoskeletal elements. *Ultramicroscopy* **17**, 31–42 (1985).
[https://doi.org/https://doi.org/10.1016/0304-3991\(85\)90174-3](https://doi.org/https://doi.org/10.1016/0304-3991(85)90174-3)
- 106 Boyle, W. S. & Smith, G. E. Charge Coupled Semiconductor Devices. *Bell System Technical Journal* **49**, 587–593 (1970).
<https://doi.org/https://doi.org/10.1002/j.1538-7305.1970.tb01790.x>
- 107 Feng, J. & Scholl, A. in *Springer Handbook of Microscopy* (eds Peter W. Hawkes & John C. H. Spence) 537–564 (Springer International Publishing, 2019).
- 108 Locatelli, A. & Bauer, E. D. Recent advances in chemical and magnetic imaging of surfaces and interfaces by XPEEM. *Journal of Physics: Condensed Matter* **20**, 093002 (2008).
- 109 Bauer, E. Surface microscopy with low energy electrons: LEEM. *Journal of Electron Spectroscopy and Related Phenomena* **241**, 146806 (2020).
<https://doi.org/https://doi.org/10.1016/j.elspec.2018.11.005>
- 110 Nordling, C., Sokolowski, E. & Siegbahn, K. Precision Method for Obtaining Absolute Values of Atomic Binding Energies. *Physical Review* **105**, 1676–1677 (1957).
<https://doi.org/10.1103/PhysRev.105.1676>
- 111 Siegbahn, K. M. Electron Spectroscopy for Atoms, Molecules and Condensed Matter. (1981).
- 112 van der Heide, P. *X-Ray Photoelectron Spectroscopy : An Introduction to Principles and Practices*. (John Wiley & Sons, Incorporated, 2011).
- 113 Baer, D. R. *et al.* Practical guides for x-ray photoelectron spectroscopy: First steps in planning, conducting, and reporting XPS measurements. *Journal of Vacuum Science & Technology A* **37** (2019). <https://doi.org/10.1116/1.5065501>

- 114 Lafferty, J. M. Boride Cathodes. *Journal of Applied Physics* **22**, 299–
309 (1951). <https://doi.org/10.1063/1.1699946>
- 115 Wolstenholme, J. & Watts, J. F. *An introduction to surface analysis
by XPS and AES*. 37-39, 50-54 (John Wiley and Sons LTd., 2003).
- 116 Greczynski, G. & Hultman, L. A step-by-step guide to perform x-ray
photoelectron spectroscopy. *Journal of Applied Physics* **132**
(2022). <https://doi.org/10.1063/5.0086359>
- 117 Greczynski, G. & Hultman, L. X-ray photoelectron spectroscopy:
Towards reliable binding energy referencing. *Progress in Materials
Science* **107**, 100591 (2020).
<https://doi.org/https://doi.org/10.1016/j.pmatsci.2019.100591>
- 118 Hüfner, S. *Photoelectron spectroscopy : principles and applications
/ Stefan Hüfner*. 3. rev. and enlarged edn, (Springer, 2003).
- 119 Renault, O. & Chabli, A. Energy-filtered Photoelectron Emission
Microscopy (EF-PEEM) for imaging nanoelectronic materials. *AIP
Conference Proceedings* **931**, 502–506 (2007).
<https://doi.org/10.1063/1.2799425>
- 120 Skallberg, A., Bunnfors, K., Brommesson, C. & Uvdal, K. New Tools
for Imaging Neutrophils: Work Function Mapping and Element-
Specific, Label-Free Imaging of Cellular Structures. *Nano Letters*
21, 222–229 (2021).
<https://doi.org/10.1021/acs.nanolett.0c03554>
- 121 Skallberg, A., Brommesson, C. & Uvdal, K. Imaging XPS and
photoemission electron microscopy; surface chemical mapping
and blood cell visualization. *Biointerphases* **12** (2017).
<https://doi.org/10.1116/1.4982644>
- 122 Lee, C.-Y., Harbers, G. M., Grainger, D. W., Gamble, L. J. & Castner,
D. G. Fluorescence, XPS, and TOF-SIMS Surface Chemical State
Image Analysis of DNA Microarrays. *Journal of the American
Chemical Society* **129**, 9429–9438 (2007).
<https://doi.org/10.1021/ja071879m>
- 123 De Carvalho, A. G. *et al.* Combining surface-sensitive microscopies
for analysis of biological tissues after neural device implantation.
Biointerphases **15** (2020). <https://doi.org/10.1116/6.0000110>
- 124 Mathieu, C. *et al.* Microscopic correlation between chemical and
electronic states in epitaxial graphene on SiC(000 $\overline{1}$).
Physical Review B **83**, 235436 (2011).
<https://doi.org/10.1103/PhysRevB.83.235436>
- 125 Andrade, H. D. *et al.* Use of energy-filtered photoelectron
emission microscopy and Kelvin probe force microscopy to

- visualise work function changes on diamond thin films terminated with oxygen and lithium mono-layers for thermionic energy conversion. *International Journal of Nanotechnology* **11**, 796–807 (2014). <https://doi.org/10.1504/ijnt.2014.063789>
- 126 Zagonel, L. F. *et al.* Orientation-dependent work function of in situ annealed strontium titanate. *Journal of Physics: Condensed Matter* **21**, 314013 (2009). <https://doi.org/10.1088/0953-8984/21/31/314013>
- 127 Renault, O. *et al.* Charge spill-out and work function of few-layer graphene on SiC(0 0 0 1). *Journal of Physics D: Applied Physics* **47**, 295303 (2014). <https://doi.org/10.1088/0022-3727/47/29/295303>
- 128 Schottky, W. H. *Physikalische zeitschrift* **15 (872)** (1914).
- 129 Lowe, D. G. Distinctive Image Features from Scale-Invariant Keypoints. *International Journal of Computer Vision* **60**, 91–110 (2004). <https://doi.org/10.1023/B:VISI.0000029664.99615.94>
- 130 Stuart, B. H. *Infrared Spectroscopy: Fundamentals and Applications*. (John Wiley & Sons, Ltd, 2004).
- 131 Peets, P., Kaupmees, K., Vahur, S. & Leito, I. Reflectance FT-IR spectroscopy as a viable option for textile fiber identification. *Heritage Science* **7**, 93 (2019). <https://doi.org/10.1186/s40494-019-0337-z>
- 132 Baker, M. J. *et al.* Using Fourier transform IR spectroscopy to analyze biological materials. *Nature Protocols* **9**, 1771–1791 (2014). <https://doi.org/10.1038/nprot.2014.110>
- 133 Martin, A. H., Meinders, M. B. J., Bos, M. A., Cohen Stuart, M. A. & van Vliet, T. Conformational Aspects of Proteins at the Air/Water Interface Studied by Infrared Reflection–Absorption Spectroscopy. *Langmuir* **19**, 2922–2928 (2003). <https://doi.org/10.1021/la0208629>
- 134 de Alwis, C., Leftwich, T. R. & Perrine, K. A. New Approach to Simultaneous In Situ Measurements of the Air/Liquid/Solid Interface Using PM-IRRAS. *Langmuir* **36**, 3404–3414 (2020). <https://doi.org/10.1021/acs.langmuir.9b03958>
- 135 Morse, P. M. Diatomic Molecules According to the Wave Mechanics. II. Vibrational Levels. *Physical Review* **34**, 57–64 (1929). <https://doi.org/10.1103/PhysRev.34.57>
- 136 González Moreno, A., López Guerrero, M. M., Vereda Alonso, E., García de Torres, A. & Pavón, J. M. C. Development of a new FT-IR method for the determination of iron oxide. Optimization of the synthesis of suitable magnetic nanoparticles as sorbent in

- magnetic solid phase extraction. *New Journal of Chemistry* **41**, 8804–8811 (2017). <https://doi.org/10.1039/C7NJ01522D>
- 137 De Meutter, J. & Goormaghtigh, E. Amino acid side chain contribution to protein FTIR spectra: impact on secondary structure evaluation. *European Biophysics Journal* **50**, 641–651 (2021). <https://doi.org/10.1007/s00249-021-01507-7>
- 138 Pakbin, B., Zolghadr, L., Rafiei, S., Brück, W. M. & Brück, T. B. FTIR differentiation based on genomic DNA for species identification of *Shigella* isolates from stool samples. *Scientific Reports* **12**, 2780 (2022). <https://doi.org/10.1038/s41598-022-06746-y>
- 139 Zancajo, V. M. R. *et al.* FTIR Nanospectroscopy Shows Molecular Structures of Plant Biominerals and Cell Walls. *Analytical Chemistry* **92**, 13694–13701 (2020). <https://doi.org/10.1021/acs.analchem.0c00271>
- 140 Windt, X. *et al.* Fourier Transform Infrared Spectroscopy for Assessing Structural and Enzymatic Reactivity Changes Induced during Feather Hydrolysis. *ACS Omega* **7**, 39924–39930 (2022). <https://doi.org/10.1021/acsomega.2c04216>
- 141 Schatten, H. *Scanning Electron Microscopy for the Life Sciences*. (Cambridge University Press, 2012).
- 142 Sawaguchi, A. Low-vacuum scanning electron microscopy for informative three-dimensional imaging of cell/tissue architectures and biomedical target localization. *Microscopy* (2026). <https://doi.org/10.1093/imicro/dfag012>
- 143 Koga, D., Kusumi, S., Shibata, M. & Watanabe, T. Applications of Scanning Electron Microscopy Using Secondary and Backscattered Electron Signals in Neural Structure. *Front Neuroanat* **15**, 759804 (2021). <https://doi.org/10.3389/fnana.2021.759804>
- 144 Wang, Y. *et al.* Neutrophil extracellular trap-microparticle complexes enhance thrombin generation via the intrinsic pathway of coagulation in mice. *Scientific Reports* **8**, 4020 (2018). <https://doi.org/10.1038/s41598-018-22156-5>
- 145 Berezin, M. Y. & Achilefu, S. Fluorescence Lifetime Measurements and Biological Imaging. *Chemical Reviews* **110**, 2641–2684 (2010). <https://doi.org/10.1021/cr900343z>
- 146 Okabe, K. *et al.* Intracellular temperature mapping with a fluorescent polymeric thermometer and fluorescence lifetime imaging microscopy. *Nature Communications* **3**, 705 (2012). <https://doi.org/10.1038/ncomms1714>

- 147 Clancy, E. *et al.* Fluorescence and phosphorescence lifetime imaging reveals a significant cell nuclear viscosity and refractive index changes upon DNA damage. *Scientific Reports* **13**, 422 (2023). <https://doi.org/10.1038/s41598-022-26880-x>
- 148 Lichtman, J. W. & Conchello, J.-A. Fluorescence microscopy. *Nature Methods* **2**, 910–919 (2005). <https://doi.org/10.1038/nmeth817>
- 149 Lakowicz, J. R. *Principles of fluorescence spectroscopy* / Joseph R. Lakowicz. Third edition edn, (Springer, 2006).
- 150 Twu, N.-C. *et al.* Spatial mapping of influenza and coronavirus receptors in the respiratory and intestinal tract epithelium of beef cattle using advanced PixF image analysis. *Scientific Reports* **15**, 44029 (2025). <https://doi.org/10.1038/s41598-025-28429-0>
- 151 Rivest, F. *et al.* Fully automated sequential immunofluorescence (seqIF) for hyperplex spatial proteomics. *Scientific Reports* **13**, 16994 (2023). <https://doi.org/10.1038/s41598-023-43435-w>
- 152 Sarott, R. C. *et al.* Development of High-Specificity Fluorescent Probes to Enable Cannabinoid Type 2 Receptor Studies in Living Cells. *Journal of the American Chemical Society* **142**, 16953–16964 (2020). <https://doi.org/10.1021/jacs.0c05587>
- 153 Thakur, S., Cattoni, D. I. & Nöllmann, M. The fluorescence properties and binding mechanism of SYTOX green, a bright, low photo-damage DNA intercalating agent. *European Biophysics Journal* **44**, 337–348 (2015). <https://doi.org/10.1007/s00249-015-1027-8>
- 154 Stokes, G. G. On the Change of Refrangibility of Light. *Philosophical Transactions of the Royal Society of London* **142**, 463–562 (1852).
- 155 Seo, J. *et al.* PICASSO allows ultra-multiplexed fluorescence imaging of spatially overlapping proteins without reference spectra measurements. *Nature Communications* **13**, 2475 (2022). <https://doi.org/10.1038/s41467-022-30168-z>
- 156 Zhang, T. Y. & Suen, C. Y. A fast parallel algorithm for thinning digital patterns. *Commun. ACM* **27**, 236–239 (1984). <https://doi.org/10.1145/357994.358023>

Papers

The papers associated with this thesis have been removed for copyright reasons. For more details about these see:

<https://doi.org/10.3384/9789181185416>

FACULTY OF SCIENCE AND ENGINEERING

Linköping Studies in Science and Technology. Dissertation No. 2518, 2026
Department of Physics, Chemistry and Biology

Linköping University
SE-581 83 Linköping, Sweden

www.liu.se